

Mapping Observations of Peptide-like molecules around Sagittarius B2*

SIQI ZHENG,^{1,2,3,†} JUAN LI,^{1,2,‡} JUNZHI WANG,^{4,§} YAO WANG,⁵ FENG GAO,^{6,7} DONGHUI QUAN,^{8,9} FUJUN DU,^{5,10}
YAJUN WU,^{1,2} EDWIN BERGIN,¹¹ AND YUQIANG LI^{1,2,3}

¹*Shanghai Astronomical Observatory, Chinese Academy of Sciences
No. 80 Nandan Road
Shanghai, 200030, China*

²*Key Laboratory of Radio Astronomy, Chinese Academy of Sciences
Nanjing 210033, China*

³*School of Astronomy and Space Sciences, University of Chinese Academy of Sciences
No. 19A Yuquan Road
Beijing 100049, People's Republic of China*

⁴*Guangxi Key Laboratory for Relativistic Astrophysics, Department of Physics, Guangxi University
Nanning 530004, PR China*

⁵ *Purple Mountain Observatory, Chinese Academy of Sciences, 10 Yuanhua Road, Nanjing 210023, People's Republic of China*

⁶ *Hamburger Sternwarte, Universität Hamburg
Gojenbergsweg 112, D-21029, Hamburg, Germany*

⁷ *Max Planck Institute for Extraterrestrial Physics (MPE), Giessenbachstr. 1, D-85748 Garching, Germany*

⁸ *Xinjiang Astronomical Observatory, Chinese Academy of Sciences, 150 Science 1-Street, Urumqi 830011, People's Republic of China*

⁹ *Research Center for Intelligent Computing Platforms, Zhejiang Laboratory, Hangzhou 311100, China*

¹⁰ *School of Astronomy and Space Science, University of Science and Technology of China, Hefei 230026, People's Republic of China*

¹¹ *Department of Astronomy, University of Michigan, Ann Arbor, MI 48109, USA*

ABSTRACT

Peptide-like molecule, which has a close connection with the origin of life, has been detected in universe. Mapping observations of HCONH₂ and CH₃CONH₂, two simplest peptide-like molecules, are performed towards Sagittarius B2 (Sgr B2) complex with the IRAM 30m telescope. Seven transitions of HCONH₂ and five transitions of CH₃CONH₂ are used in analysis. The spatial distribution of excitation temperature and column density of HCONH₂ in the molecular envelope of Sgr B2 are obtained by the rotation diagrams. Assuming the same excitation temperature as HCONH₂, the column densities of CH₃CONH₂ are also calculated. The results show that excitation temperature ranges from 6 K to 46 K in the molecular envelope of Sgr B2. The abundance ratio between HCONH₂ and CH₃CONH₂ are calculated to explore the relationship among them, as well as HNCO mentioned in our pervious research. The abundance ratio of CH₃CONH₂/HCONH₂ varies from 10% to 20%, while that of HCONH₂/HNCO ranges from 1.5% to 10%. CH₃CONH₂ is enhanced with respect to HCONH₂ in the northwest region of Sgr B2. One transition of H¹³CONH₂ is detected toward 12 positions of Sgr B2, from which a ¹²C/¹³C ratio of 28.7 is obtained. A time-dependent chemical model with a short duration of X-ray burst is used to explain the observed abundances of HCONH₂ and CH₃CONH₂, with the best fitting result at $T_{\text{dust}} = 53\text{-}56$ K. More chemical reactions are required to be included into the model since the modeled abundance is lower than the observed one at the observed T_{dust} .

Keywords: Interstellar molecules — Abundance ratios — Isotopic abundances — Molecular clouds

1. INTRODUCTION

* Released on March, 1st, 2021

† E-mail: zhengsq@shao.ac.cn

‡ E-mail: lijuan@shao.ac.cn

§ E-mail: junzhiwang@gxu.edu.cn

Peptide bond [-NH-C(O)-] is the element that links two amino acids together to form proteins. As a result, peptide-like molecules, the molecules with a structure like the peptide bond, can give us some hints into the origin of life in universe. Formamide (HCONH₂) and acetamide (CH₃CONH₂) are the smallest two peptide-like molecules. HCONH₂ has been detected in many high-mass star formation regions, comets, low-mass star formation regions and translucent cloud (e.g. López-Sepulcre et al. 2015; Colzi et al. 2021). It is regarded as the precursor of many other prebiotic molecules (Saladino et al. 2012). CH₃CONH₂ has been detected in high-mass star formation regions (e.g. Hollis et al. 2006; Halfen et al. 2011; Colzi et al. 2021), intermediate-mass protostar Serpens SMM1-a (Ligterink et al. 2022), and tentatively detected in low-mass protostar IRAS 16293-2422 (Ligterink et al. 2018). CH₃CONH₂ was only detected toward several sources, which was much less detected than that of HCONH₂.

Many chemical models have been proposed based on experiments and theoretical calculations to explain their abundance observed in ISM, including gas-phase reactions and grain surface reactions. The formation of HCONH₂ is still under discussion (see López-Sepulcre et al. (2019) for detail). Barone et al. (2015) suggested that H₂CO + NH₂ → HCONH₂ + H was an effective way for HCONH₂ to form in gas-phase reaction according to the results of their electronic structure and kinetic calculation. Skouteris et al. (2017) calculated the deuteration rate of HCONH₂ in this reaction. The results of computations were in good agreement with the observation in the hot corino of IRAS16293-2422 B. This reaction has also been used to explain the observed spatial segregation of HCONH₂ with respect to other species in shock region L1157-B1 by Codella et al. (2017). A newly proposed grain surface reaction is the reaction between CN radical and the water molecule of the ice mantle (Rimola et al. 2018). The hydrogenation of HNCO was ruled out by experiments (Noble et al. 2015), but Haupa et al. (2019) proposed a model that link HNCO and HCONH₂ with a double-cycle based on their experiment results. For CH₃CONH₂, many gas-phase reactions and grain-surface reactions have also been proposed (e.g. Quan & Herbst 2007; Quénard et al. 2018). A constant ratio between HCONH₂ and CH₃CONH₂ in various physical environments indicates that they form at an early state of star formation on the interstellar dust grains (Ligterink et al. 2022). Which kind of reactions are most important for reproducing the abundance of CH₃CONH₂ and HCONH₂ in different environment need to be constrained by more observation results.

Sagittarius B2 (hereafter Sgr B2) is an ideal place to study the chemical origin and the relationship between HCONH₂ and CH₃CONH₂, where many complex molecules have been detected to have an extended distribution and strong emission there (e.g. Jones et al. 2008; Li et al. 2017). It consists of three parts: a low density envelop, a moderate density region and molecular hotspots where the high-mass stars are forming (Hüttemeister et al. 1993). The two major high-mass star formation regions with high chemical richness are called Sgr B2(N) and Sgr B2(M). Both HCONH₂ and CH₃CONH₂ have been detected in Sgr B2(N) (Hollis et al. 2006; Halfen et al. 2011). Later, in the hot cores of it, such as Sgr B2 (N1), Sgr B2 (N2), Sgr B2 (N3), Sgr B2(N4) and Sgr B2(N5), these two molecules has also been detected and analysed (e.g. Bonfand et al. 2017; Belloche et al. 2019; Li et al. 2021). For Sgr B2(M), only HCONH₂ has been detected, while CH₃CONH₂ has not been detected (Belloche et al. 2013). The molecular envelop has an average H₂ density of $\sim 10^3$ cm⁻³, and H₂ column density of $\sim 10^{23}$ cm⁻² (Goldsmith et al. 1990). The size of it is 38 pc (15.4 ') in diameter (Scoville et al. 1975). The spatial distribution of different molecules here was found to be significantly different (e.g. Jones et al. 2008, 2011). In the molecular envelop of Sgr B2, G+0.693-0.27 (hereafter G+0.693) is a quiescent giant molecular cloud with great interest. This is a source with low excitation temperature and high levels of chemical richness (Requena-Torres et al. 2008; Zeng et al. 2018), while there is no sign of active star formation (Zeng et al. 2020). Recently, Zeng et al. (2023) detected both molecules in G+0.693. While the observation towards the hot cores and cold envelop of Sgr B2 are carried out, all of the observations mentioned above are performed toward a single position. The simultaneous mapping observation of both molecules can not only avoid the uncertainties introduced by absolute flux calibration and pointing, but also tell us how the abundance ratio varies with the environment. The spatial variation of the abundance ratio indicates the possible mechanisms that dominate the chemical networks. Besides, the physical conditions of the extended molecular envelope of Sgr B2, which remain unclear now, could be obtained with multiple transitions of these molecules.

In this paper, we present mapping observation results of HCONH₂ and CH₃CONH₂ with the IRAM 30m toward Sgr B2 complex. We study the spatial distribution and the abundance ratio of HCONH₂ and CH₃CONH₂ in Sgr B2, and the possible chemical paths would be proposed according to the abundance ratio. In Section 2, we introduce the observation and data reduction. In Section 3, we present the results of our observation. In Section 4, we make a scientific discussion about the results. The conclusions are summarised in Section 5.

2. OBSERVATION AND DATA REDUCTION

We have performed mapping observation toward Sgr B2 with the IRAM 30m telescope on Pico Veleta Spain (project 170-18) in 2019 May. The Eight MIXer Receiver and FFTs in FTS200 mode were used in position-switching mode. The observation were performed at the 3 mm band, covering a frequency range of 82.3-90 GHz. The channel spacing is 0.195 MHz, which corresponds to the velocity resolution of 0.64 km s^{-1} at 84 GHz. Pointing was checked every ~ 2 h on 1757-240, and the focus was calibrated on 1757-240 before the observation. The integration time ranges from 24 minutes to 98 minutes for different positions, with a typical system temperature of ~ 110 K, which gives a 1σ rms of 4-8 mK in T_A^* derived with the line free channels. The calibration uncertainty is within 20%.

The observing center is Sgr B2(N) ($\alpha_{J2000} = 17^h 47^m 20^s .0, \delta_{J2000} = -28^\circ 22' 19.0''$), with a sampling interval of $30''$ and a beam size of $30''$. The off position of $(\delta\alpha, \delta\beta) = (-752'', 342'')$ with respect to Sgr B2(N) was used (Belloche et al. 2013). The data were reduced with CLASS software¹. The continuum emission was subtracted via first-order polynomial fitting. The antenna temperature (T_A^*) was transformed into the main beam brightness temperature (T_{mb}) using $T_{\text{mb}} = T_A^* \cdot F_{\text{eff}} / B_{\text{eff}}$, where the forward efficiency F_{eff} is 0.95 at 3 mm, and the beam efficiency B_{eff} is attained using Ruze's equation. The spectra are smoothed to 1.35 km s^{-1} to improve the signal-to-noise ratio.

3. RESULTS

63 positions of Sgr B2 are observed to make the spatial distribution maps of target molecules. Due to the strong continuum and complex environment in Sgr B2(N) and Sgr B2(M), it would be difficult to do baseline correction and to separate the absorption or emission that comes from hot cores or the cold envelope. Therefore, the spectra of molecules in both Sgr B2(N) and Sgr B2(M) are not considered in the further analysis. Among the transitions of HCONH₂ and CH₃CONH₂, the transitions with high upper state energies are only detected around the hot cores, while in the cold envelope only transitions with low upper state energies ($E_u < 40$ K) can be detected. Besides, many transitions of the target molecules are blended with the transitions of other species due to the large line width of spectra in Sgr B2 (e.g. Belloche et al. 2013). Finally, seven transitions of HCONH₂ and five transitions of CH₃CONH₂ are selected because their emission is clean and strong enough to be detected in the cold envelop. One transition of H¹³CONH₂ are also used for analysis. The information of these transitions is listed in Table 1. The spectroscopic entries from Cologne Database for Molecular Spectroscopy (Müller et al. 2005) are used. The transition data of CH₃CONH₂ was provided by Ilyushin et al. (2004).

3.1. HCONH₂

3.1.1. Distribution of HCONH₂

The emission of HCONH₂ $1_{1,1}-0_{0,0}$, $4_{0,4}-3_{0,3}$, $4_{2,3}-3_{2,2}$, $4_{2,2}-3_{2,1}$ and $4_{1,3}-3_{1,2}$ are observed to be stronger than 3σ in 60, 63, 59, 60 and 63 positions with 1σ of about 0.01 K in T_{mb} , respectively. The emission of HCONH₂ $4_{3,2}-3_{3,1}$ and $4_{3,1}-3_{3,0}$ are observed to be weaker than other observed transitions of HCONH₂, which have the emission stronger than 3σ in 32 positions. The frequencies of these two transitions are very similar, with a difference of 2 MHz. As a result, these two transitions blended with each other, and will be solved together. The detection threshold for all transitions is 3 sigma. HCONH₂ $1_{1,1}-0_{0,0}$ is partially blended with C₂H₅CN, $v=1$, but can be separated from each other in the spectra. This is also the only one b-type transition ($\Delta K_a = \Delta K_c = \pm 1$), while others are a-type transitions ($\Delta K_a = 0$). Since the profiles of the spectra in Sgr B2 are complex (e.g. Belloche et al. 2013), which can not be fitted with a single gaussian component, the integrated intensities over a certain velocity range would be used in the following works. The integrated intensities, the first moment (the intensity-weighted velocity) and the second moment (the intensity-weighted velocity dispersion) of the transitions in different positions are listed in Table A1 and Table A2. The integrated intensity maps of each transition are shown in Figure 1 in order of increasing upper state energies. The intensities where the emission is lower than 3σ ($1\sigma \sim 0.07 \text{ km s}^{-1} \text{ K}$) are assumed to be 0. Sgr B2(N) (including Sgr B2(N1), Sgr B2(N2) and so on), Sgr B2(M) and G+0.693, where HCONH₂ has been detected, are labeled with " \times ". Because the sampling does not satisfied the Nyquist sampling criterion, the emission sizes and peak positions for different transitions are decided by eyes, which are listed in Table 2. The equivalent radius of the area where the emission is stronger than half of the emission at the peak position is used to describe the emission size.

According to Table 2 and Figure 1, the emissions of different transitions are extended in Sgr B2, while the emission size decreases with the increasing upper state energies. The shift in peak position of different transitions is significant

¹ <http://www.iram.fr/IRAMFR/GILDAS>.

comparing with the angular resolution of observations. The spectra of the observed transitions of HCONH₂ near the peak positions: Sgr B2(N) and position (30'', 60'') are displayed in Figure 2, with blue dashed lines to show the LSR velocity. The LSR velocity in each position is determined with the line profile of H¹³CCCN 10-9 in our data, considering its relatively strong emission and low optical depth. For transition with a small upper state energy, corresponding to HCONH₂ 1_{1,1}-0_{0,0}, the emission has the largest emission size, and peaks at the north cloud of Sgr B2, near position (30'', 60''). G+0.693 is located in projection 0.32 pc (or 8'') south of the position (30'', 60''), with a LSR velocity of 68 km s⁻¹ (Requena-Torres et al. 2006) and a typical lines FWHM of about 20 km s⁻¹ (Zeng et al. 2018). The observed spectra in position (30'', 60'') (see Figure 2) have a good agreement with this LSR velocity and linewidth. It has been suggested that there are large-scale, low velocity shocks (Henshaw et al. 2016; Zeng et al. 2020). Many molecules have been found to be enhanced there, such as HNC, HCO₂⁺ and CH₃OH (e.g. Minh et al. 1998; Jones et al. 2008). The low velocity shocks in G+0.693 might be a possible explanation for the emission peak there. When the upper state energy increases, such as HCONH₂ 4_{0,4}-3_{0,3} and 4_{1,3}-3_{1,2}, the peak moves to the west of Sgr B2(M), near position (-30'', -60''). The equivalent radius of emission region is ~ 55'' for these two transitions. If the upper state energy is higher, like HCONH₂ 4_{2,3}-3_{2,2}, 4_{2,2}-3_{2,1}, HCONH₂ 4_{3,2}-3_{3,1} and 4_{3,1}-3_{3,0}, the emission has the smaller emission size than other transitions, and peaks near Sgr B2(N). Sgr B2(N) is a source with many complex organic molecules (COMs) detected to have high column density and high excitation temperature. Most of the molecules there emit in the LSR velocity of ~ 63-64 km s⁻¹ and 73-74 km s⁻¹, with a linewidth of 7 km s⁻¹ for each velocity component (Belloche et al. 2013). This is consistent with the spectra in Figure 2. Similar variation between the distribution of different transitions has been mentioned by Jones et al. (2008) and Jones et al. (2011). Such variation among different transitions reflects the complex excitation environment there, which would be analysed by rotation diagrams in Section 3.1.3.

3.1.2. isotopic species

The emission of H¹³CONH₂ 4_{0,4}-3_{0,3} is also detected in the observation as listed in Table 1. In addition to Sgr B2(N), H¹³CONH₂ 4_{0,4}-3_{0,3} has an emission stronger than 3 σ in 11 positions. The spectra are shown in Figure 3, with the spectra of HCONH₂ 4_{0,4}-3_{0,3} as a comparison to investigate whether this transition is optically thick. The spectra of HCONH₂ 4_{0,4}-3_{0,3} are divided by 25, 20, 15 and 3 to compare with the spectra of H¹³CONH₂ in different positions. The ¹²C/¹³C ratio can also be obtained from those two transitions. The integrated intensity map is drawn to find out its spatial distribution (see Figure 4). The distribution of H¹³CONH₂ 4_{0,4}-3_{0,3} in the extended envelope is found to have a similar morphology with that of HCONH₂ 4_{0,4}-3_{0,3}. In comparison, the emission of H¹³CONH₂ 4_{0,4}-3_{0,3} peaks in Sgr B2(N) while that of HCONH₂ 4_{0,4}-3_{0,3} is weak, implying the emission around there is optically thick.

With the emission of isotope species detected in multiple positions, the isotope ratio ¹²C/¹³C in the region can be obtained from the intensity ratio of H¹³CONH₂ and HCONH₂ 4_{0,4}-3_{0,3}. Here we assume that the abundance ratio of HCONH₂ to H¹³CONH₂ has the same values as the intensity ratio, considering their similar upper state energies (E_u). Another assumption is that the ratio of ¹²C to ¹³C is equal to the abundance ratio of HCONH₂ and H¹³CONH₂, namely, there is no isotope fraction. The isotope ratio is assumed to be a constant value in Sgr B2. Based on these assumptions, the intensity ratio between HCONH₂ and H¹³CONH₂ is equal to the ratio of ¹²C to ¹³C if the transitions used are optically thin. In Table 3, the intensity ratios of HCONH₂ 4_{0,4}-3_{0,3} to H¹³CONH₂ 4_{0,4}-3_{0,3} in the positions where H¹³CONH₂ 4_{0,4}-3_{0,3} is detected are listed. Since HCONH₂ 4_{0,4}-3_{0,3} is probably optically thick, a larger intensity ratio and the intensity ratio in the positions with large distance from hot cores can reflect the isotope ratio better. Therefore, position (0'', -60'') and (0'', 0'') are excluded when analysing the isotope ratio. Position (0'', 90'') is also excluded because of its extremely large intensity ratio.

The ratio of ¹²C/¹³C obtained from the intensity ratio is about 26 to 33, indicating the assumption of a constant ratio in the envelope of Sgr B2 is reasonable. To obtain the ¹²C/¹³C ratio of the envelope, the emission of H¹³CONH₂ 4_{0,4}-3_{0,3} in the region far away from the hot cores are averaged. After averaging the spectra, the signal-to-noise ratio raises and the emission of H¹³CONH₂ can then be detected to be stronger than 3 σ (1 σ = 1.8 mK) in the region shown within the blue square frame in Figure 4. The averaged spectra of HCONH₂ 4_{0,4}-3_{0,3} and H¹³CONH₂ 4_{0,4}-3_{0,3} are shown in Figure 5. The spectra are integrated in the same velocity range which is marked with red window in the figure. The ratio between the intensities of these two lines is 28.7 ± 1.7 (listed in the last line of Table 3), within the uncertainty of the result calculated from single position, which can be regarded as the ¹²C/¹³C ratio of the envelope.

The optical depths (τ) of HCONH₂ 4_{0,4}-3_{0,3} can then be calculated from the isotope ratio according to the following formula:

$$\frac{I_{\text{HCONH}_2}}{I_{\text{H}^{13}\text{CONH}_2}} = \frac{1 - \exp(-\tau)}{1 - \exp(-\frac{\tau}{12\text{C}/13\text{C}})} \quad (1)$$

. where I_{HCONH_2} and $I_{\text{H}^{13}\text{CONH}_2}$ are the integrated intensities of HCONH_2 $4_{04}\text{-}3_{03}$ and $\text{H}^{13}\text{CONH}_2$ $4_{04}\text{-}3_{03}$. The results are listed in the last column of Table 3. In the envelope of Sgr B2, only the emission in position (0'', -60'') has a relatively large τ of 0.51. For the other positions, the emission is optically thin. The much smaller ratio in position (0'', 0''), where Sgr B2(N) is located, gives a large τ of 5.30. Part of the emission there comes from the hot cores, which is difficult to be separated from the component of the envelope around. The strong continuum and high molecular abundance of the hot core may be a reason accounting for such larger τ . Due to its complexity, we would not put emphasis on this position and may pay more attention to the positions in the cold extended envelope (further discussion in Section 4.1).

3.1.3. Rotation diagram

As seven transitions of HCONH_2 have been detected in most of the regions in Sgr B2, the column densities and excitation temperature of HCONH_2 toward different positions can be attained with rotation diagrams. The intensities of transition HCONH_2 $4_{0,4}\text{-}3_{0,3}$ are corrected with the optical depth obtained from the $^{12}\text{C}/^{13}\text{C}$. The other transitions are regarded to be optically thin under the LTE assumption, and a single temperature could be used to describe the energy level populations in the area.

The transitions that are lower than 3 σ levels would not be used in fitting, but they would be labeled in the diagrams with an arrow to represent their 3 σ upper limits. Rotation diagrams can be drawn according to the formula (Herbst & van Dishoeck 2009):

$$\frac{N_u}{g_u} = \frac{N_{tot}}{Q(T_{rot})} e^{-\frac{E_u}{T_{rot}}} = \frac{8\pi k\nu^2 I}{hc^3 A_{ul} g_u} \quad (2)$$

where N_u is the column density of upper energy level, g_u is the upper state degeneracy, N_{tot} is the total column density, T_{rot} is the rotation temperature, $Q(T_{rot})$ is the partition function, E_u is the upper state energy, I is the intensity, c is the velocity of light, and A_{ul} is the emission coefficient. T_{rot} is equal to excitation temperature (T_{ex}) under the LTE assumption. $Q(T_{rot})$ is the function of T_{rot} , calculated by the formula: $Q(T_{rot}) = \sum g_i e^{E_i/kT_{rot}}$. The calibration error is not included into the error of intensities because the calibration error is small enough to be omitted after averaging the spectra of each scan. Since the emission is more extended than the telescope beam according to the distribution map of different transitions, a filling factor correction is not considered.

The transition HCONH_2 $1_{1,1}\text{-}0_{0,0}$ is not included in all of the diagrams because it deviated too much from the fitted straight line in the rotation diagram of every position. This deviation can be the result of its different transition type from other lines, which is a b-type transition. It is likely that the a-type transitions and b-type transitions of HCONH_2 is not thermalized there. If the point of the b-type transition is located near the fitting line, the intensity of it in each position needs to be about 10 times weaker than what it is now. Therefore, the column density obtained from the b-type transition would be one magnitude larger than that obtained from a-type transitions. This phenomenon has also been observed by Nummelin et al. (2000) and Zeng et al. (2018). Because the transitions of a-type and b-type couple together, namely both type of transitions can be produced from the same upper energy level, we regard the a-type and b-type as two different temperature components of HCONH_2 . For position (30'', 60''), the excitation temperature of b-type transitions in G+0.693, which is 3.7 ± 0.7 K (Zeng et al. 2018), can be used to calculate the column density of b-type transition there. The obtained column density of b-type transition there is $1.14 \pm 0.23 \times 10^{15} \text{cm}^{-2}$. The column density of a-type transitions derived from the rotation diagram is $1.3 \pm 0.3 \times 10^{14} \text{cm}^{-2}$ with an excitation temperature of 13.1 ± 3.0 K. The total column density in this position is $1.27 \pm 0.26 \times 10^{15} \text{cm}^{-2}$ taking into account both a-type and b-type transitions. The ratio of b-type to a-type transitions is 8.8. For other positions, only one b-type transition is detected. The rotation diagram is not available to deal with both types of the transition separately. So, we only give the column densities of HCONH_2 with a-type transitions. The significant difference between the excitation temperature and column density of both type transitions perhaps suggests that transitions with different types trace different physical regions.

In some positions, such as Sgr B2(N) and Sgr B2(M), there is absorption and seriously blending from other molecules. Therefore, these positions are not used to draw the rotation diagram. In addition, position (90'', 120'') and (90'', 90'') are also not used as these two positions would produce fake information in the distribution map. Position (30'', 150''), (-120'', -30'') and (-120'', -60'') are not used as well due to the low intensities of more than 2 transitions.

Only 54 positions are used to draw the rotation diagrams. The selected positions are shown with green "x" in Figure 6. The rotation diagrams are shown in Figure A1 and Figure A2, corresponding to the positions with HCONH_2

4_3-3_2 detected and not detected. Since HCONH_2 $1_{1,1}-0_{0,0}$ is not included in the fit, it is labeled as an orange square, while other transitions are labeled as blue circles. From the results of rotation diagrams, the distribution of column densities and excitation temperature could be obtained. The results are shown in Figure 7 and Table 4. The values at the positions not labeled in Figure 6 are interpolated from the values around them, which do not have physical meanings. According to the figure, the T_{ex} of HCONH_2 range from 6 K to 46 K, with higher values around the hot cores. The column densities of HCONH_2 calculated with only a-type transitions range from 0.2 to $4.6 \times 10^{14} \text{cm}^{-2}$. More details about the rotation diagrams are discussed in section 4.2.

3.2. CH_3CONH_2

3.2.1. distribution

Because of the internal rotation of methyl group, CH_3CONH_2 has A- and E- species. In our observations, only CH_3CONH_2 -A has relatively clean and strong emission. The frequencies of the used CH_3CONH_2 -A transitions are similar, with a difference of 2.7 MHz ($\sim 9.3 \text{ km s}^{-1}$, a smaller line width than the typical line width in Sgr B2). Therefore, those transitions will also be used together. The column densities for all positions are measured with the emission of CH_3CONH_2 -A. The transitions of CH_3CONH_2 -A are observed to be stronger than 3σ in 30 positions. The spectra of CH_2CONH_2 in all the positions with emission stronger than 3σ levels are shown in Figure 8, with the spectra of HCONH_2 $4_{22}-3_{21}$ overlapped on them. The dashed blue lines are used to show the LSR velocity of the position. In the extended cold envelope, the profiles of the spectra of HCONH_2 and CH_3CONH_2 were similar to each other in the same position, from which we can assume these transitions were excited from the same cloud.

The integrated intensity map of CH_3CONH_2 is shown in Figure 9. All the transitions of CH_3CONH_2 -A listed in Table 1 are used to draw the map. The intensities are assumed to be 0 in the positions where the emission is lower than 3σ levels. The emission size and the peak position are listed in Table 2. The transitions of CH_3CONH_2 have similar emission sizes as that of HCONH_2 $4_{0,4}-3_{0,3}$, while it peaks near Sgr B2(N). The distribution of emission in the envelope of Sgr B2 is similar to the transitions of HCONH_2 , which may imply that these two molecules are chemically or physically linked.

3.2.2. Column density

As the detected clean transitions of CH_3CONH_2 blend with each other, the column densities and excitation temperature can not be obtained by rotation diagrams. As a results, the column densities are calculated using the detected transitions together, assuming the same excitation temperature as HCONH_2 .

Since the difference between the upper state energies of different transitions is small, which is 19.82 K and 18.77 K for 8-7 A and 7-6 A respectively, they have a similar sensitivity to the excitation temperature. Namely, the column densities calculated from these transitions will not deviate too much if we assume they have the same upper state energy. Thus, a common upper state energy is used to simplify the calculation. Because the transitions CH_3CONH_2 8-7 A have larger dipole moment (see in Table 1), the emission of them would be stronger than that of CH_3CONH_2 7-6 A. Most of the error is also generated by transitions CH_3CONH_2 8-7 A. Therefore, the upper state energy of CH_3CONH_2 8-7 A (19.82 K) is chosen as the upper state energy to avoid the complexity of calculation. The column densities are calculated with the following formula (Pillai et al. 2007):

$$N_{\text{tot}} = \frac{N_u}{g_u} \times Q(T_{\text{ex}}) \times \exp(E_u/kT_{\text{ex}}) = \frac{3h}{8\pi^3 S \mu^2} \times \frac{I \times Q(T_{\text{ex}})}{J_\nu(T_{\text{ex}}) - J_\nu(T_{\text{bg}})} \times \frac{J(T_{\text{ex}})}{\eta_\nu} \quad (3)$$

where E_u is the upper state energy, μ^2 is the dipole moment, and S is the line strength. The value of $\mu^2 S$ is obtained from the sum of each transition. η_ν is the beam filling factor, which is set to be 1 because the emission of CH_3CONH_2 is extended.

The results are listed in Table 4. For the position where the emission of CH_3CONH_2 is not detected, the upper limits of column densities is given. The column densities of CH_3CONH_2 range from 0.6 to $7.6 \times 10^{13} \text{cm}^{-2}$. The distribution of column density is shown in Figure 10, with the distribution map of the column densities of HCONH_2 as comparison. The column densities where CH_3CONH_2 are not detected are set to be 0. According to the figure, the distributions of both molecules have an extended distribution and increase rapidly around hot cores. The abundance ratio with respect to HCONH_2 is discussed in section 4.3.

4. DISCUSSION

4.1. isotopic species

From the intensity ratio of HCONH_2 to $\text{H}^{13}\text{CONH}_2$ (in Table 3), the derived ratio of ^{12}C to ^{13}C is 28.7 ± 1.7 in Sgr B2. This ratio is consistent with previous researches which obtain a ratio of 25 ± 8 and 31 ± 8 from the two components of HCONH_2 in Sgr B2(N) (Halfen et al. 2017), and the average ratio of 24 ± 7 and 23 ± 6 obtained from the two components of 7 different molecules in Sgr B2(N), but slightly higher than the ratio of ~ 25 obtained from CH_3OH in Sgr B2 (N2) (Müller et al. 2016).

However, this ratio is just the ratio obtained from the region in the west of Sgr B2. The emission of $\text{H}^{13}\text{CONH}_2$ $4_{04}-3_{03}$ is too weak to be detected in the averaged spectra in other regions of Sgr B2. More observations are required to do a further study about the $^{12}\text{C}/^{13}\text{C}$ ratio in the envelope of Sgr B2.

4.2. rotation diagram

With the rotation diagrams of HCONH_2 , the excitation temperature in the envelope of Sgr B2 is obtained, which ranges from 6 to 46 K. The rotation diagram of HCONH_2 has also been derived toward Sgr B2(N) by Halfen et al. (2011). They have detected a wide range of transitions with E_u ranging from 10 K to 200K. Their results show that both molecules have a cold extended component and a hot component. In our observation, only transitions with low E_u (< 40 K) are used to draw the rotation diagram. Therefore, only one cold component is obtained in each position.

Based on the results about the ^{12}C and ^{13}C in the section 4.1, the assumption that all the transitions of HCONH_2 are optically thin might not be correct in all positions. If the emission is optically thick, the intensity of the transition would be underestimated, which would lead to an underestimated column density and an overestimated of T_{ex} . For the positions near Sgr B2(N) and Sgr B2(M), an absorption led by the strong continuum there could also influence the results.

In addition, drawing rotation diagrams need the assumption that T_{bg} could be omitted comparing with T_{ex} and the Rayleigh-Jeans law is valid (i.e. $h\nu \ll kT$), so that equation 3 could be transferred to equation 2. However, T_{ex} in positions at the boundary of our observing area, such as position ($30''$, $120''$), the obtained excitation temperatures are lower than 10 K. Combined with the high frequencies of transitions, the Rayleigh-Jeans law can be hardly satisfied. In this case, the column densities obtained by the rotation diagrams would be underestimated. The column densities were $\sim 30\%$, $\sim 17\%$ and $\sim 10\%$ larger than the results obtained in section 3.1 when T_{ex} is 7 K, 10 K, and 14 K, respectively.

Besides, the rotation diagrams are drawn only with a-type transitions. The only detected b-type transition has a much stronger intensity than it should be if both types can reach thermalization. Thus, the excitation temperature of b-type transition can not be assumed to be same as that of a-type. Here we only give the column densities based on the a-type transitions. To include b-type transitions into the analysis, more observations are needed.

It is found that the excitation temperatures in the envelope are smaller than the dust temperature, implying that these molecules are sub-thermalized. In this instance, a non-LTE method would be a better way to calculate the excitation temperatures and column densities. However, the energy population can be well described with one single excitation temperature for the a-type transitions of HCONH_2 . Therefore, the column densities are still reliable and non-LTE effect will not affect our results too much.

4.3. Abundance ratio

To further study the relationship between CH_3CONH_2 and HCONH_2 , the abundance ratio of them are calculated. HNCO would also be included in the discussion according to our former research (Zheng et al. 2022). Assuming the same excitation temperature as HCONH_2 , the column densities could be obtained by the same way as CH_3CONH_2 . In Sgr B2(M) and Sgr B2(N), there are many hot cores, as well as strong continuum emissions, which make the spectra difficult to be handled. Thus, the abundance ratio toward these two positions would not be included in the discussion.

The distribution maps of the column density ratio are displayed in Figure 11. From the figure, the abundance ratios between CH_3CONH_2 and HCONH_2 are found to range from 10 % to 20 %, except for one position with a smaller ratio, and two positions with larger ratios. The two positions with the ratios larger than 20% are marked with yellow triangles in the left panel of Figure 11. The spectra of those two molecules in these two positions are shown in Figure 8. In those figures, the spectra of HCONH_2 $4_{22}-3_{21}$ is chosen to compare with the spectra of CH_3CONH_2 , because they have a similar E_u . Thus, the comparison between those spectra can reflect the abundance ratio to some extent. The ratio of CH_3CONH_2 to HCONH_2 maximizes at position ($-30''$, $90''$), with the values of 25.7%. This constant ratio in most of the positions indicates that they have the same response to the physical or chemical environment. Perhaps,

there is a chemical or physical link between CH_3CONH_2 and HCONH_2 . The ratio between HCONH_2 and HNCO range from 1.5% to 10.5%. The distribuion has a similar feature with the distribuion of excitation temperature, imply a possible relationship between the excitation temperature and the reactions that connect these two molecules.

To compare the results with other sources, the abundance with respect to H_2 are calculated. We use the Hi-GAL 350, 250, and 70 μm maps. the values are the averaged values in a $30''$ beam to match the beam of IRAM 30m at 3 mm. Figure 12 shows the abundances with respect to H_2 . The blue lines are the power-law fits of the observed positions, which are given by the equation $X(\text{CH}_3\text{CONH}_2)=0.55 \times X(\text{HCONH}_2)^{1.06}$ with a Pearson coefficient of 0.79, and $X(\text{HCONH}_2)=0.0017 \times X(\text{HNCO})^{0.84}$ with a Pearson coefficient of 0.39. The dotted pink, dash-dotted purple and dashed orange line correspond to the power-law fits given by López-Sepulcre et al. (2015), $X(\text{HCONH}_2) = 0.04 \times X(\text{HNCO})^{0.93}$, by Quénard et al. (2018), $X(\text{HCONH}_2) = 32.14 \times X(\text{HNCO})^{1.29}$, and by Colzi et al. (2021), $X(\text{HCONH}_2) = 0.006 \times X(\text{HNCO})^{0.73}$. The red points in the figure show the abundance of HCONH_2 and HNCO in Sgr B2 (N2) (Bonfand et al. 2019), G10.47+0.03 (Gorai et al. 2020), G31.41+0.31 (Colzi et al. 2021). The data used to fit the pink dotted lines in López-Sepulcre et al. (2015) include only the compact/inner solution of rotation diagram analyses in shocks and star formation regions with different masses. The sources used in Quénard et al. (2018) include shocks and hot corinos. The line obtained in our work lies below the other three lines, implying a relatively low abundance of HCONH_2 comparing with HNCO in the extended envelope. The low Pearson coefficient of 0.39 also indicates the weak relationship between HNCO and HCONH_2 . It is likely that the formation mechanism of these molecules are different in the envelope compared with the mechanism in the compact sources. This conclusion has a good agreement with the lower panel of Figure 2 of López-Sepulcre et al. (2015). For the line between HCONH_2 and CH_3CONH_2 , a nearly linear relationship needs to be explained with an updated chemical model.

Some uncertainties may affect the final results. First, the critical densities vary with molecules, leading to the difference in excitation temperature. If the excitation temperature of CH_3CONH_2 is lower than HCONH_2 , it would result in a lower column density of CH_3CONH_2 and a smaller abundance ratio. Besides, only the clean transitions of CH_3CONH_2 -A are detected. The emission of CH_3CONH_2 -E, which may help to attain more accurate column density, is too weak or blend with other molecules. What's more, the low signal to noise ratio due to the low abundance of CH_3CONH_2 may also affect the abundance ratio obtained from the integrated intensity. Therefore, an observation with higher resolution, higher sensitivity and wider bandwidth are needed in the future.

4.4. Some special positions

Sgr B2(N): It is a massive star-formation region with many compact molecular cores and strong continuum. Since there is strong continuum, the spectra in Sgr B2(N) are not analyzed. The results in Sgr B2(N) drawn in the figures that describe the spatial distribution of excitation temperature and abundance ratio are the results of interpolation based the position besides, and thus can not reflect the exact physical condition there. From the integrated intensity maps of the transitions of both molecules, the peaks for transitions with relatively higher upper state energies and the peak of the transition of isotopic species are located in Sgr B2(N), which indicates the high column density here. Halfen et al. (2011) found that the column densities of HCONH_2 and CH_3CONH_2 towards Sgr B2(N) are $5.6 \times 10^{14} \text{ cm}^{-2}$ and $6.9 \times 10^{14} \text{ cm}^{-2}$. Therefore, the column densities of HCONH_2 and CH_3CONH_2 should peak in Sgr B2(N). For the ratio of $\text{HCONH}_2/\text{HNCO}$, the results attained by ALMA show that the column density of HNCO , HCONH_2 , CH_3CONH_2 in Sgr B2(N2) is $2 \times 10^{18} \text{ cm}^{-2}$, $2.6 \times 10^{18} \text{ cm}^{-2}$, and $1.4 \times 10^{17} \text{ cm}^{-2}$, respectively (Belloche et al. 2017). The ratio of $\text{HCONH}_2/\text{HNCO}$ is 130%. In Sgr B2(N3), Sgr B2(N4), Sgr B2(N5), the abundance ratio of HCONH_2 to HNCO is 25%, <56% and 44%, respectively (Bonfand et al. 2017). The abundance ratio is higher than our results, implying a different mechanism there. The trend that the ratio of HCONH_2 to HNCO increases with the excitation temperature (see Figure 7 and Figure 11) is consistent with the larger ratio found in Sgr B2(N). In terms of $\text{CH}_3\text{CONH}_2/\text{HCONH}_2$, the abundance ratio in Sgr B2(N1E) and Sgr B2(N1) is 9% and 15% (Li et al. 2021). In Sgr B2(N2), Belloche et al. (2017) found the abundance ratio of $\text{CH}_3\text{CONH}_2/\text{HCONH}_2$ to be 5.4%. In Sgr B2(N1S), the abundance ratio of $\text{CH}_3\text{CONH}_2/\text{HCONH}_2$ is 14% (Belloche et al. 2019). The abundance ratio obtained from the hot core is consistent with that in the cold envelope.

Sgr B2(M): It is a hot core at a later stage than Sgr B2(N). The continuum there is stronger and consist of more dense cores than Sgr B2(N) (Schmiedeke et al. 2016). The linewidths of the spectra there range from ~ 6 to 15 km s^{-1} and the LSR velocity is 60 to 66 km s^{-1} (Belloche et al. 2013). An obvious absorption in the spectrum of HCONH_2 4_{04} - 3_{03} and a slight absorption in the spectrum of HCONH_2 4_{13} - 3_{12} are detected there, while CH_3CONH_2 was not detected. Perhaps the CH_3CONH_2 here has been destroyed or the spectrum have strong absorption.

G+0.693: Among our observation positions, (30'', 60'') is the nearest from G+0.693. In position (30'', 60''), the column density of CH₃CONH₂ is $2.6 \times 10^{13} \text{ cm}^{-2}$, while HCONH₂ is $1.3 \times 10^{14} \text{ cm}^{-2}$. The abundance ratio of HCONH₂/HNCO and CH₃CONH₂/HCONH₂ is 3.9% and 19.2%, respectively. In the observation of Zeng et al. (2018), the ratio of HCONH₂/HNCO is 20%. If only a-HCONH₂ is considered, the ratio is 1.6%. In the work of Zeng et al. (2023), the column density of HCONH₂ is calculated from the isotope species H¹³CONH₂, which is $2.5 \times 10^{14} \text{ cm}^{-2}$. The ¹²C/¹³C ratio they used is 40, which is larger than our result of 28.7. The column density of HCONH₂ is consequently larger than the column density we obtain. Because multiple transitions of CH₃CONH₂, they obtain the excitation temperature of 7.4 K and 7.8 K for CH₃CONH₂-A and CH₃CONH₂-E, lower than the temperature we used. If the same excitation temperature is used, a similar column density of CH₃CONH₂-A can be obtained. The abundance ratio in their work is 46%, considering both CH₃CONH₂-A and CH₃CONH₂-E.

4.5. Chemical model

To investigate the synthesis mechanism of peptide-like molecules HCONH₂ and CH₃CONH₂ in the region extending among 100'' from Sgr B2, we study the evolution of HCONH₂ and CH₃CONH₂ in chemical models. The simulations provided by Wang et al. (2021) are adopted for comparing with observations, since most observed positions still locate in the low-density envelope around Sgr B2 (Hüttemeister et al. 1993, 1995; Schmiedeke et al. 2016), for which the chemical evolution had been calculated via Monte Carlo method and explained different distributions of seven complex organic molecules (COMs). Besides CH₂OHCHO, CH₃OCHO, t-HCOOH, C₂H₅OH, CH₃NH₂, CH₃OCH₃, and C₂H₅CN analyzed by Wang et al. (2021), HCONH₂ and CH₃CONH₂ are already included in the chemical reaction network. Figure 13 presents the relationship between the abundance $X(\text{CH}_3\text{CONH}_2)$ (with respect to H₂) and $X(\text{HCONH}_2)$, and the relationship between $X(\text{HCONH}_2)$ and $X(\text{HNCO})$ in the best-fit model (the same one as proposed by Wang et al. (2021)) comparing with observations, while the other models cannot fit observations. The corresponding physical evolution is that the low density extended region around Sgr B2 ($n_{\text{H}} = 2 \times 10^3 \text{ cm}^{-3}$) underwent a cold phase with gas and dust temperature $T_{\text{gas}} = T_{\text{dust}} = 10 \text{ K}$, then a warm-up phase of increasing both temperatures simultaneously to reach the maximum 200 K, including an X-ray flare from Sgr A* with a short duration of no more than 100 yr when $T_{\text{gas}} = T_{\text{dust}} = 20 \text{ K}$ (for details see Table 1 and Section 3.2.2 in Wang et al. (2021)). Under such circumstance, simulated $X(\text{CH}_3\text{CONH}_2)$, $X(\text{HCONH}_2)$, and $X(\text{HNCO})$ can match observed abundances at $T_{\text{dust}} \sim 53 - 56 \text{ K}$, 105 - 115 K, and 170 - 190 K, respectively. However, considering the relatively low dust temperature $T_{\text{dust}} \sim 20 - 30 \text{ K}$ in the extended envelope according to the dust continuum, our chemical models still need to be further modified.

We leave rectification of the chemical reaction network for a future detailed study. Here we only discuss those reactions that are key for the species concern us here and need to be further assessed. According to current simulations, the most important reactions for producing HCONH₂, CH₃CONH₂, and HNCO at $T_{\text{dust}} \sim 53 - 56 \text{ K}$ are JNH₂ + JHCO → HCONH₂, JNH₂ + JCH₃CO → CH₃CONH₂, and JHNCO → HNCO, respectively, and the letter J represents species on the grain. Therefore, the reactive desorption driven by exothermic reactions (Garrod et al. 2007; Vasyunin & Herbst 2013) is the most significant mechanism for producing HCONH₂ and CH₃CONH₂ in relatively cold environment, which is also concluded for the other seven COMs (Wang et al. 2021). For HNCO which has already been synthesized abundantly on the grain surface, the thermal desorption is the main mechanism for increasing its gaseous abundance since its evaporation temperature is about 50 K.

Similarly, the thermal desorption induces rapidly increasing abundances of HCONH₂ and CH₃CONH₂ at $T_{\text{dust}} \sim 105 - 115 \text{ K}$, which exceeds their evaporation temperatures (about 93 K and 105 K, respectively, calculated with the binding energies of 5556 K and 6281 K presented by Garrod (2013) and via equation (6) presented by Du et al. (2012)). In addition, the gaseous ion-molecule reactions involving C⁺ are the main approach for depleting HCONH₂ and CH₃CONH₂ molecules in the warm-up phase, which is similar to seven COMs (Wang et al. 2021). These reactions may explain the evolution of HCONH₂ and CH₃CONH₂ in the region close to Sgr B2(N) and Sgr B2(M) with higher density and temperature. Nevertheless, for producing enough HCONH₂ and CH₃CONH₂ molecules at $T_{\text{dust}} \sim 20 - 30 \text{ K}$ in the extended envelope, more efficient non-thermal desorption mechanisms need to be investigated in the future analysis, not only reactive desorption but also photodesorption and Eley-Rideal mechanism (Garrod et al. 2007; Öberg et al. 2010; Cernicharo et al. 2012; Vasyunin & Herbst 2013; Vastel et al. 2014; Ruaud et al. 2015).

Besides non-thermal desorption processes, other reasons can cause the discrepancy between best-fit dust temperatures derived from simulations and observations. 1) The uncertainties of many parameters for calculating reaction rates in chemical models are large, especially the binding energy (or desorption energy) of each species (Penteado et al. 2017). For example, in this chemical reaction network, the adopted binding energies of HCONH₂ and HNCO are 5556 K and

2850 K originating from OSU network database and Garrod (2013), while new calculated values 5468 K and 4684 K using the Gaussian 09 suite of programs show a smaller difference (Gorai et al. 2020), which may induce their evolution to become similar. Additionally, contrast to the adopted fix values in most chemical models for simplicity, the binding energies measured by laboratory experiments vary with the coverage of grain surface (He et al. 2016; Behmard et al. 2019). The binding energy distributions are also inferred by theoretical computations (Ferrero et al. 2020; Perrero et al. 2022) and significantly influence the efficiencies of thermal desorption and grain surface two-body reactions (Penteado et al. 2017; Grassi et al. 2020), which may increase the abundances of HCONH₂ and CH₃CONH₂ at $T_{\text{dust}} \sim 20 - 30$ K. 2) Some new reactions for synthesizing HCONH₂ and CH₃CONH₂ may have not been considered in aforementioned models. One reaction is the gas-phase reaction $\text{NH}_2 + \text{H}_2\text{CO} \rightarrow \text{HCONH}_2 + \text{H}$, which has been used to explain the observation toward the shock region L1157-B1 (Codella et al. 2017). The dual-cyclic hydrogen addition and abstraction reactions between HNCO and HCONH₂ in ice grains derived from experiments (Haupa et al. 2019) are not included, neither. Thus, more accurate chemical simulations adopting binding energy distributions and new reactions are necessary to fit observed abundances in the envelope around Sgr B2 with low dust temperature in the future study. 3) The aforementioned models have not adopted multiple physical mechanisms simultaneously to investigate whether an individual mechanism can induce a good fit comparing with observations. However, the environment of Sgr B2 is complex, more sophisticated physical model including not only X-ray flare from Sgr A* (Marin et al. 2023) but also shocks should be considered in simulations. Such accurate physical model demands more observations to limit it.

5. SUMMARY

We have performed mapping observation toward Sgr B2 to further study the spatial distributions of the peptide-like molecules and the relationship between them. The obtained results are listed there:

1. HCONH₂ and CH₃CONH₂ are detected to have an extended distribution toward Sgr B2, with the abundance ratio range from 10% to 20%. The abundance of CH₃CONH₂ was enhanced toward to north-west of Sgr B2. The excitation temperature in the envelop of Sgr B2 ranges from 6K to 46 K, based on the rotation diagram of HCONH₂.

2. The isotopic molecule H¹³CONH₂ is also detected toward 12 positions of Sgr B2. The emission of H¹³CONH₂ 4₀₄-3₀₃ indicated that HCONH₂ 4₀₄-3₀₃ has absorption toward Sgr B2(N). The ratio of ¹²C/¹³C is 28.7 toward Sgr B2 envelope.

3. A chemical model including a cold phase and a warm-up phase with a short duration X-ray burst of no more than 100 yr at $T_{\text{gas}} = T_{\text{dust}} = 20$ K is used to explain the observed abundances of HCONH₂ and CH₃CONH₂. The simulations can fit observed abundances at $T_{\text{dust}} \sim 53 - 56$ K, 105 - 115 K, and 170 - 190 K, respectively. The reactive desorption driven by exothermic reactions dominate the synthesis of these two peptide-like molecules in relatively cold environment. Such dust temperatures are still higher than observations, which requires more accurate chemical models for explaining it.

This work is based on observations carried out under project number 170-18 with the IRAM 30m telescope. IRAM is supported by INSU/CNRS (France), MPG (Germany) and IGN (Spain). This work has been supported by the National Key R&D Program of China (No. 2022YFA1603101). This work is also supported by CDMS database. We thank JinJin Xie for the suggestions for the draft. YW acknowledges the support by the Natural Science Foundation of Jiangsu Province (Grant Number BK20221163).

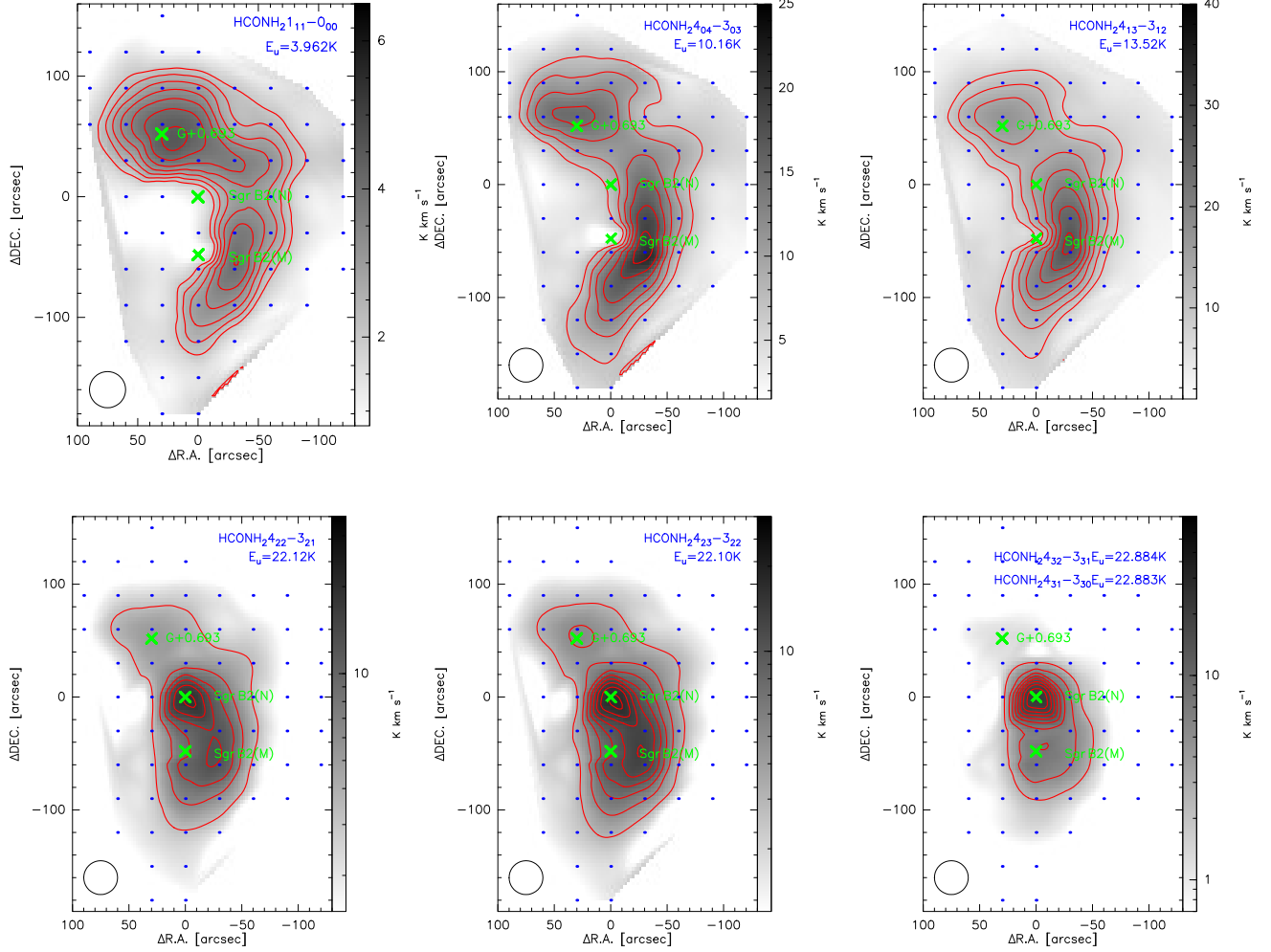


Figure 1. The gray-scale and contours show the spatial distribution of different transitions of HCONH₂. The figures are listed in order of increasing upper state energy. The first figure is the map of HCONH₂ 1_{1,1}-0_{0,0} at 82549.562 MHz. The contour levels start at 2 K km s⁻¹ with a step of 0.4 K km s⁻¹. The second figure is the map of HCONH₂ 4_{0,4}-3_{0,3} at 84542.330 MHz. The contour levels start at 7 K km s⁻¹ with a step of 2.5 K km s⁻¹. The third figure is the map of HCONH₂ 4_{1,3}-3_{1,2} at 87848.874 MHz. The contour levels start at 8.4 K km s⁻¹ with a step of 3 K km s⁻¹. The fourth figure is the map of HCONH₂ 4_{2,2}-3_{2,1} at 85093.272 MHz. The contour levels start at 3.3 K km s⁻¹ with a step of 3 K km s⁻¹. The fifth figure is the map of HCONH₂ 4_{2,3}-3_{2,2} at 84807.795 MHz. The contour levels start at 3 K km s⁻¹ with a step of 2 K km s⁻¹. The sixth figure is the map of HCONH₂ 4_{3,2}-3_{3,1} and 4_{3,1}-3_{3,0} at 84888.994 MHz and 84890.987, respectively. The contour levels start at 2.5 K km s⁻¹ with a step of 2.5 K km s⁻¹. Sgr B2(N), Sgr B2(M), and G+0.693 are labeled with "x". The beam size are shown in the left corner of each panel.

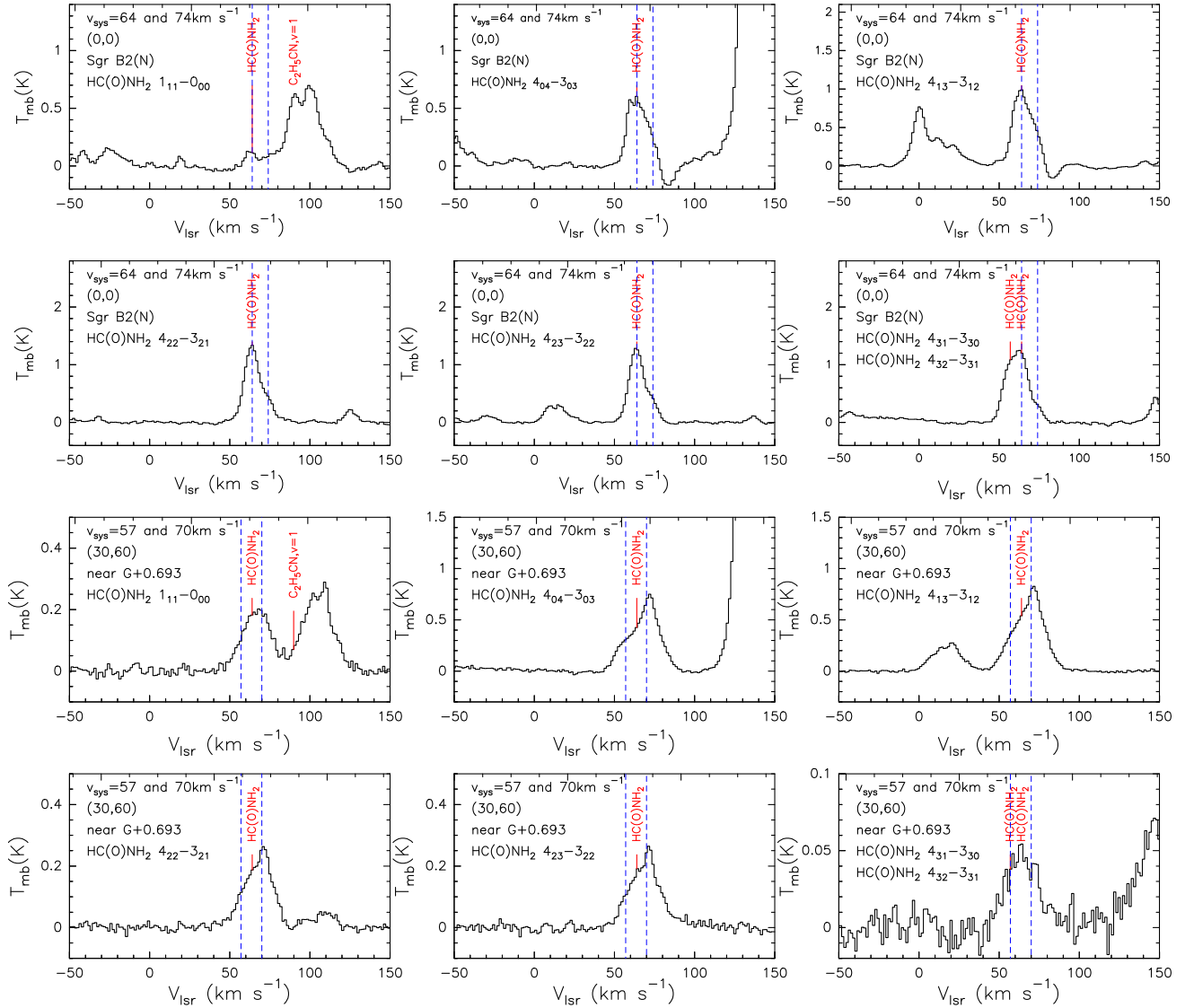


Figure 2. The spectra of HCONH_2 in position (30, 60) and Sgr B2(N). Frequencies are indicated with the red lines above the spectra. The v_{sys} , determined by H^{13}CCCN 10-9, are labeled with blue dashed lines. The value of v_{sys} is labeled in the top left corner of each panel.

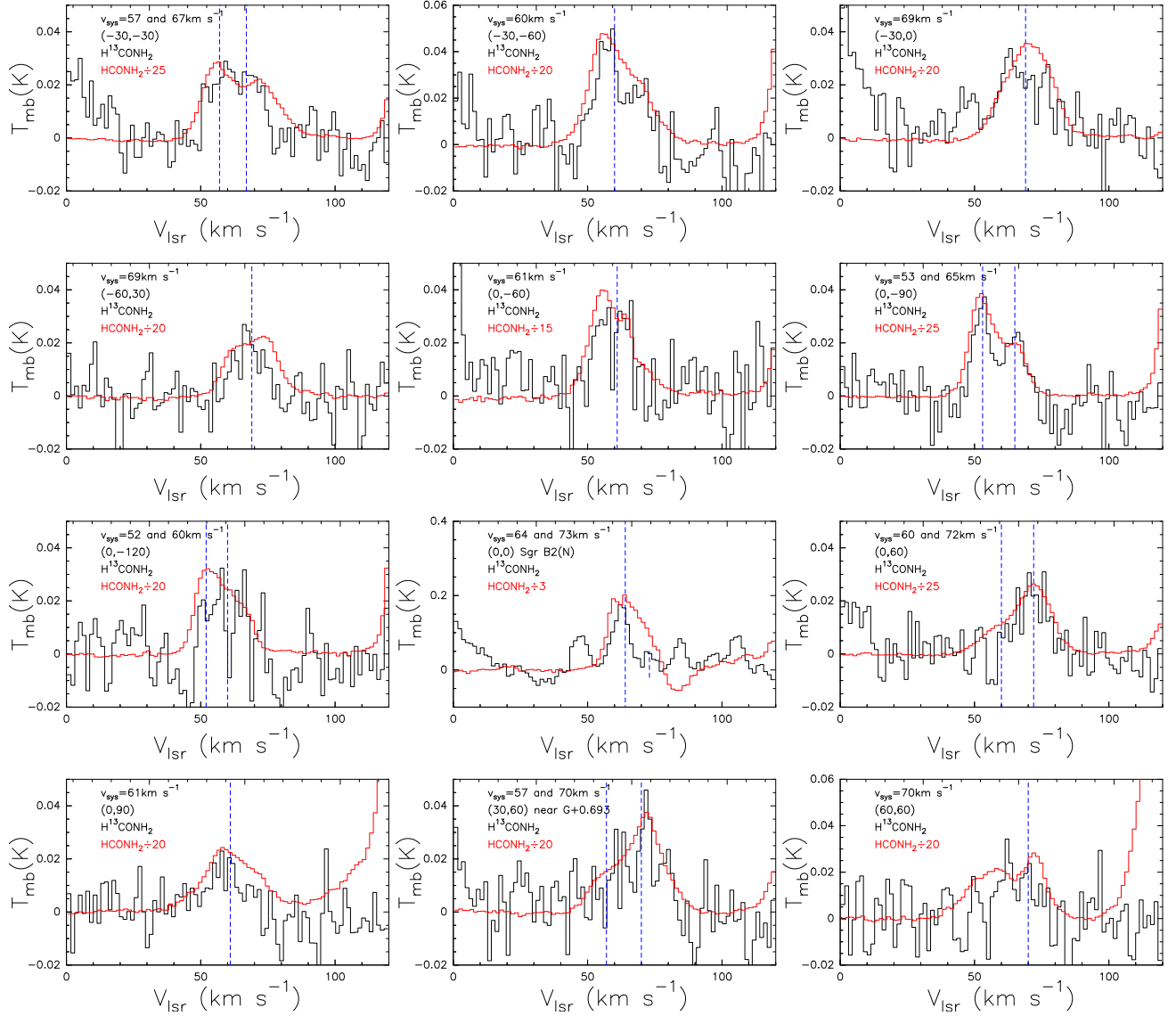


Figure 3. The spectra of HCONH_2 $4_{04}\text{-}3_{03}$ and $\text{H}^{13}\text{CONH}_2$ $4_{04}\text{-}3_{03}$. The v_{sys} are labeled with blue dashed lines. The spectra of HCONH_2 $4_{04}\text{-}3_{03}$ are divided by 25, 20, 15 and 3 to compare with the spectra of $\text{H}^{13}\text{CONH}_2$ in different positions. The value of v_{sys} is labeled in the top left corner of each panel.

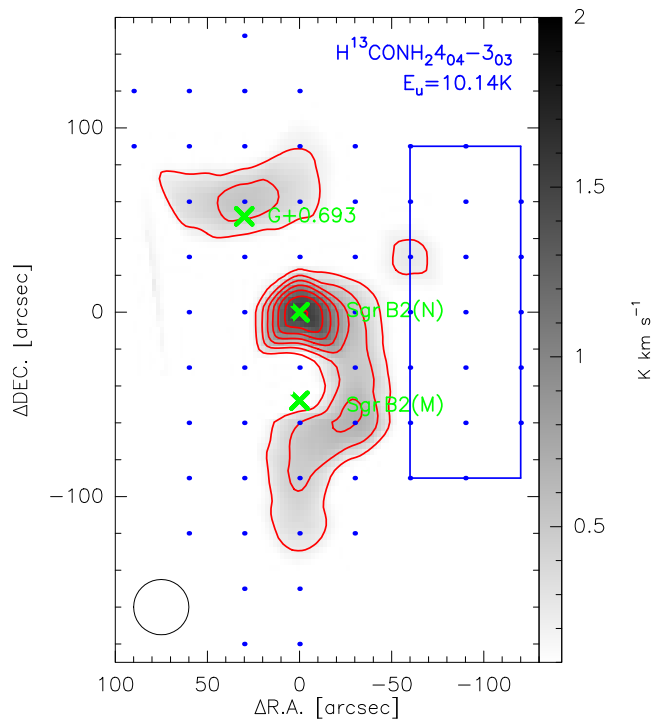


Figure 4. The distribution of $\text{H}^{13}\text{CONH}_2$ $4_{04}-3_{03}$ at 84390.679 MHz. The contour map starts from 5σ with the step of 5σ . 1σ is about 0.43 K km s^{-1} . Sgr B2(N) and Sgr B2(M) are labeled with "x". Beam size is shown in the bottom left corner. The area in the blue square shows the region used to average the spectra of the $\text{H}^{13}\text{CONH}_2$.

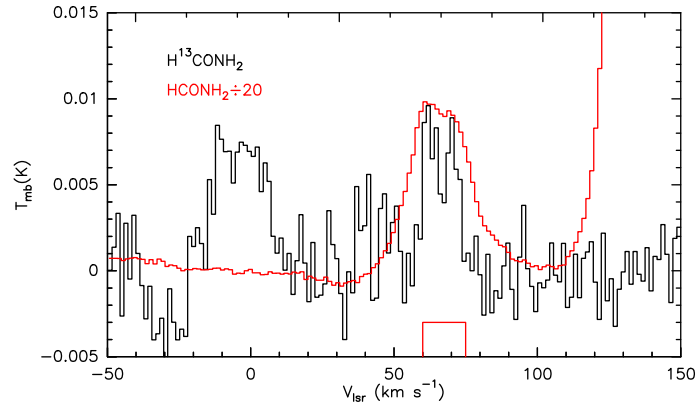


Figure 5. The averaged spectra of the $\text{H}^{13}\text{CONH}_2$ in the right region of Sgr B2. The red window represents the integrated velocity range, which is 60 km s^{-1} to 75 km s^{-1} .

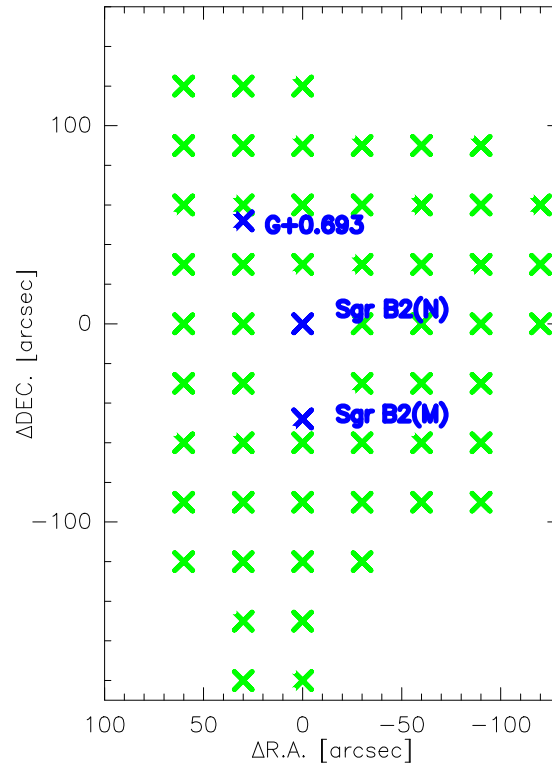


Figure 6. The positions selected to draw rotation diagrams. The selected position are labeled with green "x". Sgr B2(N), Sgr B2(M), and G+0.693 are labeled as blue "x".

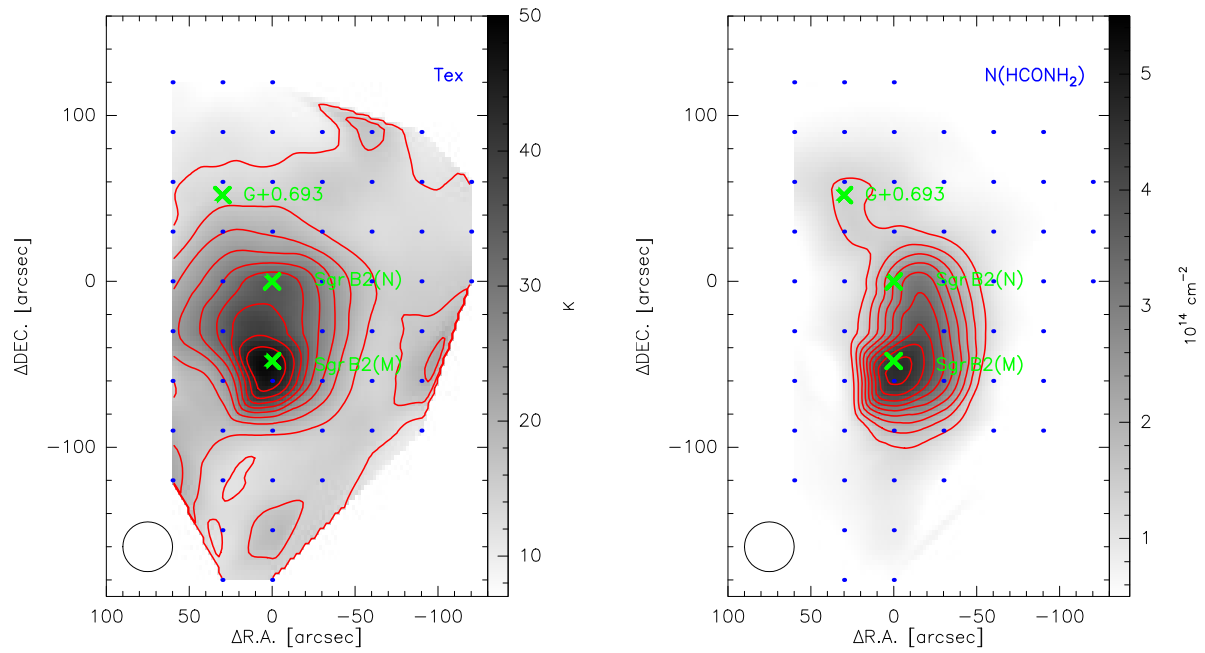


Figure 7. The distribution of excitation temperature and column density of HCONH₂. The contour levels of the left panel start at 12 K with a step of 4 K. The contour levels of the right panel start at $1.3 \times 10^{14} \text{ cm}^{-2}$ with a step of $0.4 \times 10^{13} \text{ cm}^{-2}$.

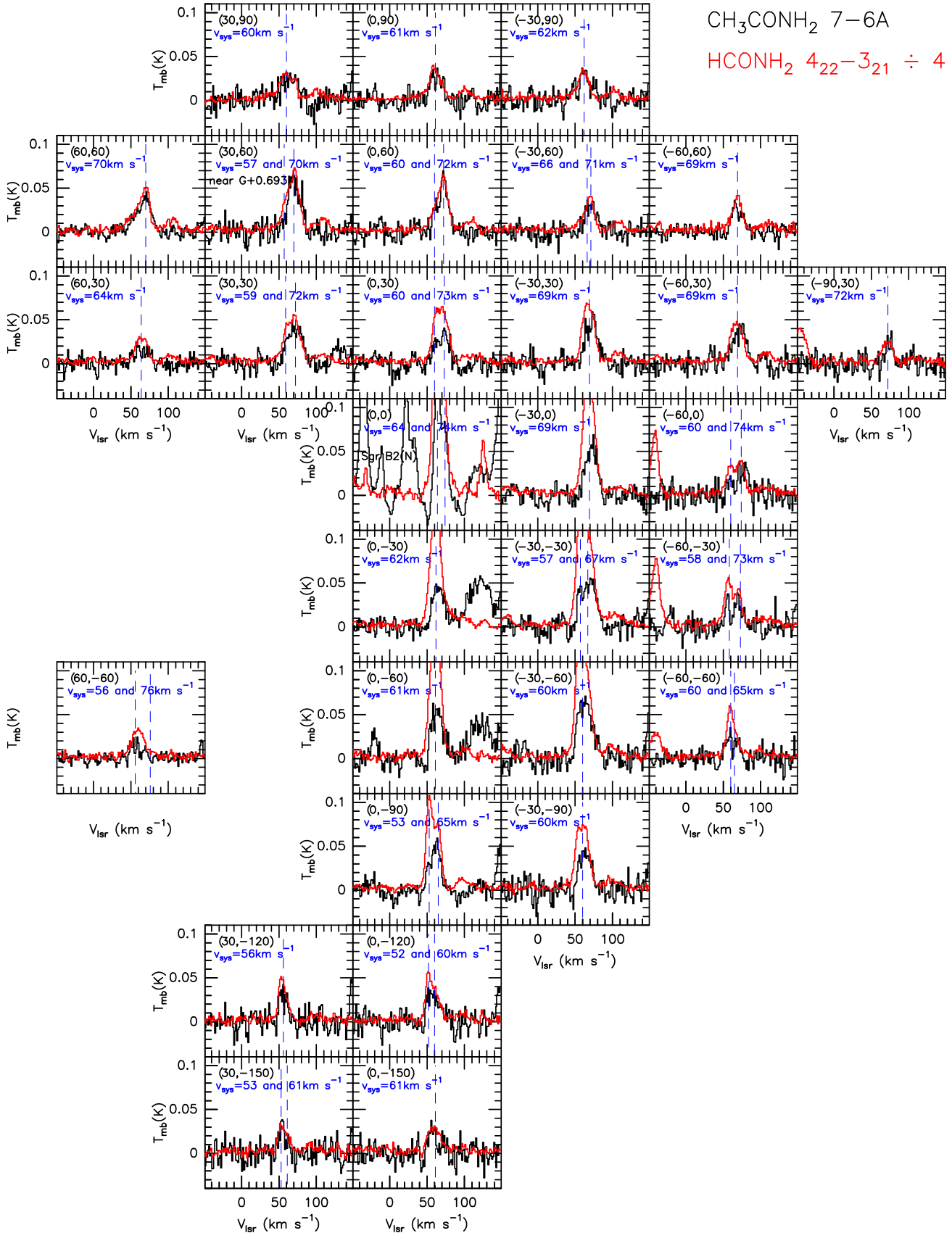
CH₃CONH₂ 8–7ACH₃CONH₂ 7–6AHCONH₂ 4₂₂–3₂₁ ÷ 4

Figure 8. The spectra of CH₃CONH₂ and HCONH₂ 4₂₂–3₂₁ in Sgr B2. The red profiles correspond to the spectra of HCONH₂ 4₂₂–3₂₁, while the black profiles are the spectra of CH₃CONH₂. The positions are labeled in the top left corner. The v_{sys} in difference positions are labeled with blue dashed lines. The value of v_{sys} is labeled in the top left corner of each panel.

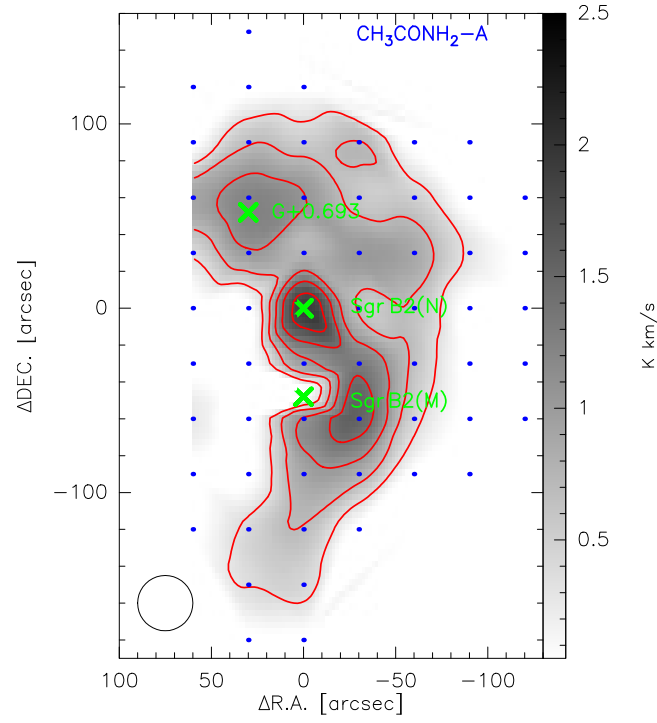


Figure 9. The integrated intensity map of CH_3CONH_2 emission. The integrated intensities of five transitions listed in Table 1 were used together to plot the map. The contour levels of CH_3CONH_2 emission start at 5σ with a step of 5σ . $\sigma \approx 0.07 \text{ km s}^{-1} \text{ K}$ for this map. Sgr B2(N), Sgr B2(M), and G+0.693 are labeled with "x". Beam size is shown in the bottom left corner.

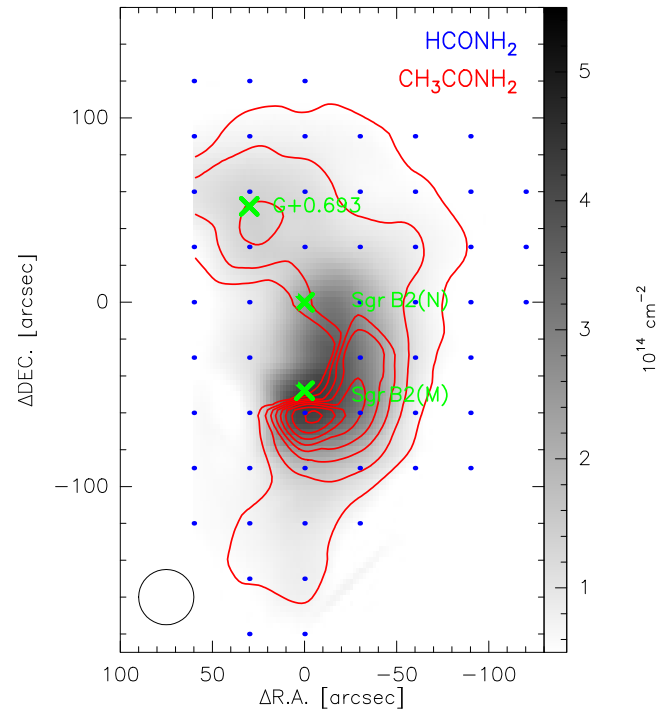


Figure 10. The distribution of column densities in Sgr B2. The gray-scale and the contour level represent the column density of HCONH_2 and CH_3CONH_2 respectively. The contour levels start at $0.7 \times 10^{13} \text{ cm}^{-2}$ with the step of $1 \times 10^{14} \text{ cm}^{-2}$.

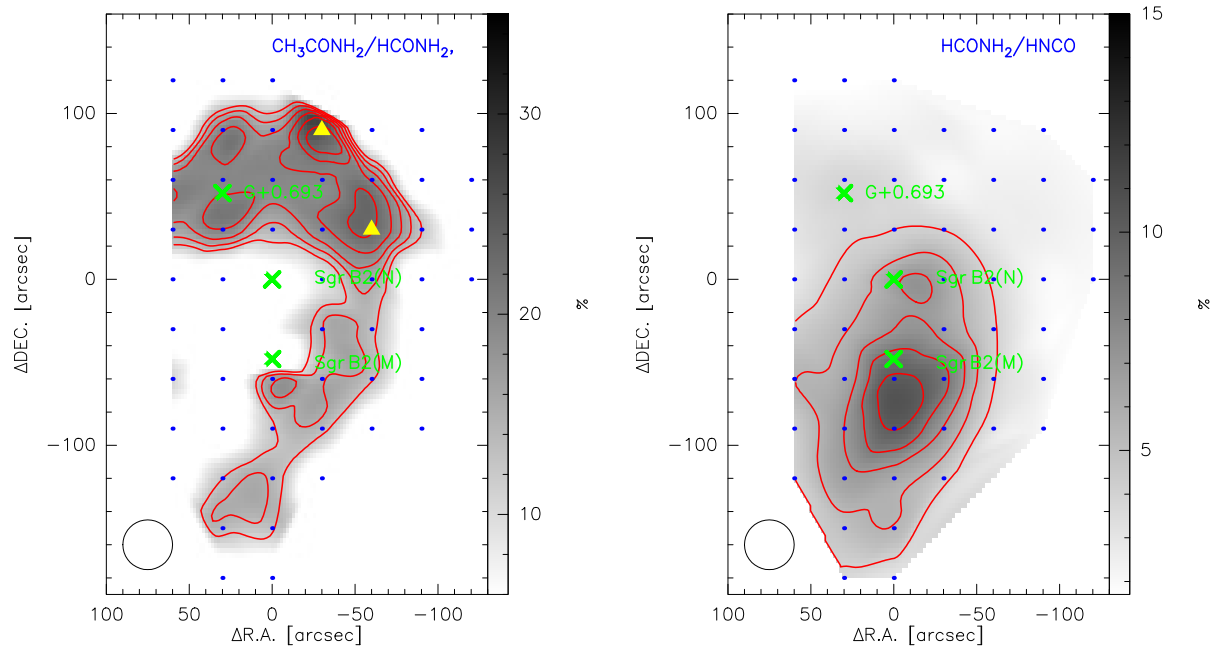


Figure 11. The distribution of the ratio between CH_3CONH_2 , HCONH_2 and HNCO . The left figure corresponds to the ratio of CH_3CONH_2 to HCONH_2 , of which the contour levels start at 12.5% and increase in steps of 2.5%. The positions with the ratios larger than 20% were pointed out with the yellow triangles. The figure in the right is ratio of HCONH_2 to HNCO , of which the contour levels start at 4% and increase in steps of 1.5%.

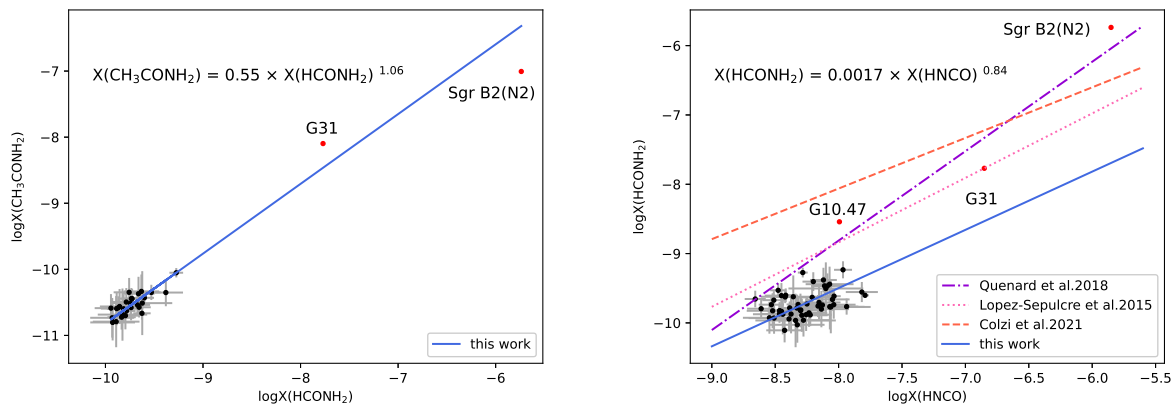


Figure 12. The abundance of HCONH_2 , CH_3CONH_2 , and HNCO , with respect to H_2 . The blue lines are the power-law fitted results in our work. The dotted pink, dash-dotted purple and dashed orange line in the right panel are the results of López-Sepulcre et al. (2015), Quénard et al. (2018), and Colzi et al. (2021). The red points in the figure show the abundance of HCONH_2 and HNCO in Sgr B2 (N2) (Bonfand et al. 2019), G10.47+0.03 (Gorai et al. 2020), G31.41+0.31 (Colzi et al. 2021). The black points are the observed abundances measured in the different positions of Sgr B2 complex.

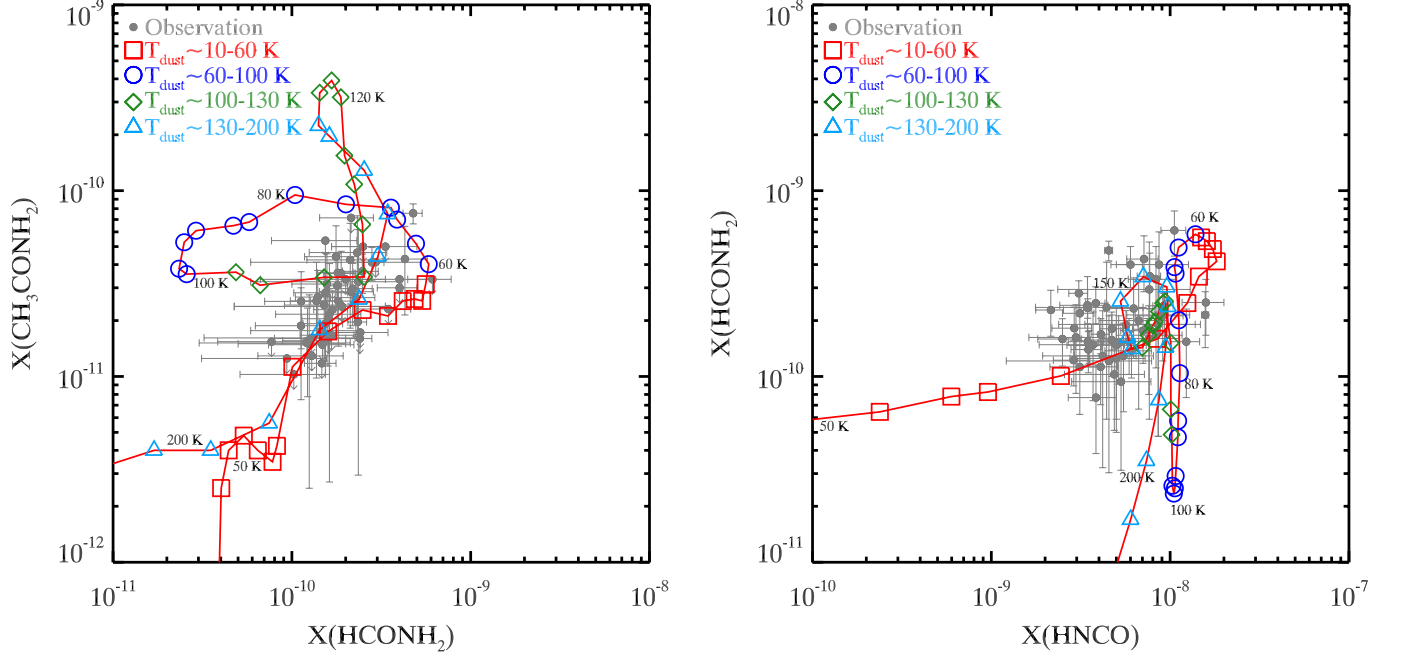


Figure 13. Comparison of observed abundances of CH_3CONH_2 , HCONH_2 , and HNCO (with respect to H_2) with simulated abundances using the best-fit chemical model in Wang et al. (2021). The red solid lines represent the evolution of $X(\text{CH}_3\text{CONH}_2)$ versus $X(\text{HCONH}_2)$ and $X(\text{HCONH}_2)$ versus $X(\text{HNCO})$ at different time in the warm-up phase; the dust temperature at a few selected points are labelled. The results for $T_{\text{dust}} \sim 10 - 60$ K, $60 - 100$ K, $100 - 130$ K, and $130 - 200$ K are plotted as squares, circles, diamonds, and triangles, respectively. The best-fit model is an evolving model with the following parameters: $n_{\text{H}} = 2 \times 10^3 \text{ cm}^{-3}$, $A_{\text{V}} = 10$, the duration of the cold phase $t_{\text{cold}} = 3 \times 10^5 \text{ yr}$, the duration of the warm-up phase $t_{\text{warmup}} = 2 \times 10^5 \text{ yr}$, the maximum temperature after the warm-up $T_{\text{max}} = 200 \text{ K}$, the external UV radiation scaling factor $G_0 = 10^4$ with an X-ray burst at $T_{\text{gas}} = T_{\text{dust}} = 20 \text{ K}$ (the total timescale $t_{\text{total}} = 3.459 \times 10^5 \text{ yr}$), the effective ionization rate $\zeta_{\text{CR}} = 1.3 \times 10^{-13} \text{ s}^{-1}$ and the duration $t = 10^2 \text{ yr}$ (for details see Table 1 and Section 3.2.2 in Wang et al. (2021)).

Table 1. The transitions of HCONH₂ and CH₃CONH₂

Molecule	Transition	Rest Freq. MHz	E_u K	$\log_{10}(A)$ s^{-1}	$\mu^2 S$ D^2	Comments	Reference
HCONH ₂	1 _{1,1} -0 _{0,0}	82549.562	3.962	-5.8001	0.726	Partially blend with C ₂ H ₅ CN,v=1.	
	4 _{0,4} -3 _{0,3}	84542.330	10.16	-4.3888	52.279	No blend.	
	4 _{2,3} -3 _{2,2}	84807.795	22.10	-4.5094	39.227	No blend.	
	4 _{3,2} -3 _{3,1}	84888.994	37.00	-4.7422	22.884	No blend.	(1)
	4 _{3,1} -3 _{3,0}	84890.987	37.01	-4.7422	22.883	No blend.	
	4 _{2,2} -3 _{2,1}	85093.272	22.12	-4.5051	39.227	No blend.	
	4 _{1,3} -3 _{1,2}	87848.874	13.52	-4.3666	49.030	No blend.	
H ¹³ CONH ₂	4 _{0,4} -3 _{0,3}	84390.679	10.14	-4.3912	52.259	No blend.	(1)
CH ₃ CONH ₂ -A	7 _{2,6,0} -6 _{1,5,0}	87629.757	18.77	-	65.860	No blend.	
	8 _{0,8,0} -7 _{1,7,0}	87632.434	19.82	-	94.010	No blend.	
	8 _{1,8,0} -7 _{1,7,0}	87632.443	19.82	-	5.868	No blend.	(2)
	8 _{0,8,0} -7 _{0,7,0}	87632.501	19.82	-	5.868	No blend.	
	8 _{1,8,0} -7 _{0,7,0}	87632.510	19.82	-	94.010	No blend.	

Note: The transitions of HCONH₂ and CH₃CONH₂ used for mapping. For CH₃CONH₂, only A-species were detected. Col. (1) chemical formula; Col. (2) transition quantum number (Belloche et al. 2013); Col. (3) rest frequency; Col. (4): upper state energy level (K); Col. (5): emission coefficient; Col. (6): μ^2 is the dipole moment, and S is the line strength; Col. (7) comments. Reference: (1) Kryvda et al. (2009), (2) Ilyushin et al. (2004)

Table 2. The emission size and peak position of HCONH₂ and CH₃CONH₂

molecule	transition	peak position	emission size
			"
HCONH ₂	1 _{1,1} -0 _{0,0}	(19, 47)	81
	4 _{0,4} -3 _{0,3}	(-29, -55)	53
	4 _{1,3} -3 _{1,2}	(-29, -52)	57
	4 _{2,2} -3 _{2,1}	(-4, -4)	37
	4 _{2,3} -3 _{2,2}	(-5, -5)	38
	4 _{3,2} -3 _{3,1}	(0, 0)	20
	4 _{3,1} -3 _{3,0}		
CH ₃ CONH ₂ -A	7 _{2,6,0} -6 _{1,5,0}	(-4, -3)	47
	8 _{0,8,0} -7 _{1,7,0}		
	8 _{1,8,0} -7 _{1,7,0}		
	8 _{0,8,0} -7 _{0,7,0}		
	8 _{1,8,0} -7 _{0,7,0}		
	8 _{1,8,0} -7 _{0,7,0}		

Note: the emission size listed in Col(3) is defined by the equivalent radius of the area where the emission is stronger than half of the emission at the peak position.

Table 3. The intensity ratio between $\text{H}^{13}\text{CONH}_2$ and HCONH_2

position	Velocity range km s^{-1}	$I_{\text{H}^{13}\text{CONH}_2}$ K km s^{-1}	I_{HCONH_2} K km s^{-1}	ratio %	τ
(0, -60)	48 75	0.44(0.08)	9.93(0.11)	22.7(4.0)	0.51
(-30, 0)	55 85	0.54(0.05)	14.28(0.10)	26.4(2.5)	0.18
(-30, -30)	50 80	0.52(0.05)	15.81(0.10)	30.7(2.7)	0.04
(0, 60)	50 86	0.34(0.05)	12.73(0.07)	37.9(6.0)	0
(30, 60)	50 85	0.53(0.08)	14.29(0.09)	27.2(3.9)	0.11
(-60, 30)	58 80	0.26(0.05)	8.15(0.08)	31.3(5.9)	0
(-30, -60)	48 78	0.67(0.07)	18.64(0.10)	27.9(3.1)	0.06
(0, 90)	45 85	0.21(0.06)	11.02(0.14)	51.8(15.6)	0
(0, -90)	45 70	0.46(0.05)	14.66(0.07)	31.9(3.1)	0
(0, -120)	48 78	0.31(0.6)	11.11(0.07)	35.3(7.2)	0
(60, 60)	48 78	0.36(0.07)	11.98(0.08)	33.3(6.2)	0
(0, 0)	55 78	1.53(0.17)	8.96(0.09)	5.9(0.7)	5.30
west Sgr B2	60 75	0.09(0.01)	2.7(0.02)	28.7(1.7)	

Table 4. Column density of HCONH₂ and CH₃CONH₂

rac	decl	T _{ex}	N _{HCONH₂}	N _{CH₃CONH₂}	N _{HNCO}	r(CH ₃ CONH ₂ /HCONH ₂)	r(HCONH ₂ /HNCO)
"	"	K	×10 ¹⁴ cm ⁻²	×10 ¹³ cm ⁻²	×10 ¹⁵ cm ⁻²	%	%
-60	-60	14.2±4.0	0.8±0.2	1.0±0.4	1.8±0.4	12.9	4.1
30	0	27.8±11.9	0.9±0.3	≤ 0.6	2.0±0.3	≤ 7.0	4.4
-30	0	26.3±5.0	2.5±0.4	2.3±0/4	4.1±0.3	9.1	6.3
0	30	19.4±4.5	1.4±0.3	1.9±0.5	3.4±0.4	14.3	4.0
-30	30	15.9±4.9	1.2±0.3	2.3±0.9	3.0±0.6	19.4	4.0
-30	-30	27.2±8.8	3.1±0.7	4.6±1.1	4.8±0.6	14.8	6.5
30	30	19.7±11.6	1.3±0.6	2.6±1.5	3.5±1.1	19.9	3.8
30	-30	33.4±14.0	1.1±0.3	≤ 0.6	1.9±0.3	≤ 5.7	5.4
0	60	13.4±4.0	1.1±0.4	2.2±1.0	3.3±0.8	19.6	3.5
60	0	18.9±13.1	0.3±0.2	≤ 0.5	1.0±0.4	≤ 16.6	2.8
-60	0	16.3±7.9	0.9±0.4	1.5±0.9	2.5±0.8	15.7	3.8
0	-60	46.1±15.8	4.6±0.7	7.6±1.2	4.5±0.4	16.7	10.2
30	60	13.1±3.0	1.3±0.3	2.6±0.9	3.4±0.6	19.6	3.9
-30	60	15.5±6.9	0.7±0.2	1.3±0.8	3.1±0.9	19.6	2.2
60	30	12.3±3.7	0.5±0.2	0.8±0.4	1.7±0.4	16.5	3.0
-60	30	12.9±3.6	0.8±0.3	1.8±0.8	2.9±0.7	22.7	2.8
60	-30	23.1±15.1	0.4±0.2	≤ 0.6	1.0±0.3	≤ 15.6	4.2
-60	-30	15.5±5.5	1.1±0.3	1.4±0.7	2.6±0.6	13.3	4.2
30	-60	23.2±8.6	0.8±0.2	≤ 0.6	1.2±0.2	≤ 7.2	6.2
-30	-60	24.0±7.4	3.2±0.7	4.8±1.3	3.6±0.5	15.2	8.9
-90	0	14.8±9.8	0.3±0.2	≤ 0.4	1.7±0.8	≤ 11.7	2.1
0	90	9.9±1.5	0.7±0.1	1.2±0.4	2.9±0.5	16.9	2.4
0	-90	17.3±5.3	1.8±0.5	2.1±0.8	1.7±0.3	12.1	10.1
60	90	9.5±1.0	0.6±0.1	≤ 0.4	2.3±0.3	≤ 6.7	2.6
30	90	10.8±3.5	0.7±0.3	1.4±0.8	3.0±0.9	19.6	2.4
-30	90	10.0±2.3	0.6±0.2	1.5±0.7	2.4±0.6	25.7	2.5
-60	90	16.7±18.7	0.4±0.3	≤ 0.5	1.8±1.3	≤ 14.2	2.0
-90	90	9.7±3.5	0.3±0.1	≤ 0.4	1.3±0.5	≤ 16.5	2.0
60	-90	19.4±15.6	0.6±0.3	≤ 0.5	1.3±0.6	≤ 9.8	4.3
30	-90	16.9±7.6	0.7±0.3	≤ 0.5	1.0±0.3	≤ 6.5	7.0
-30	-90	15.3±4.3	1.4±0.4	1.9±0.7	2.0±0.4	13.6	6.9
-60	-90	14.8±10.8	0.4±0.3	≤ 0.5	1.3±0.7	≤ 12.0	3.2
-90	-90	10.2±3.3	0.2±0.1	≤ 0.4	1.0±0.3	≤ 21.5	2.1
-90	30	13.0±7.5	0.5±0.3	0.6±0.6	2.0±0.9	12.6	2.5
-90	60	11.9±6.2	0.4±0.2	≤ 0.4	1.7±0.8	≤ 9.5	2.4
-120	0	15.7±14.6	0.4±0.3	≤ 0.5	1.8±1.1	≤ 14.4	2.0
-120	30	12.3±7.1	0.4±0.2	≤ 0.4	1.9±0.9	≤ 10.8	2.2
-120	60	12.5±5.9	0.3±0.1	≤ 0.3	1.5±0.6	≤ 11.7	2.0

Note. Col(1) and Col(2): the equatorial offsets of emission with respect to Sgr B2(N); Col(3): the excitation temperature; Col(4): the column densities of HCONH₂; Col(5): the column densities of CH₃CONH₂; Col(6): the column densities of HNCO; Col(7): the column density ratio of CH₃CONH₂ to HCONH₂. Col(8): the column density ratio of HCONH₂ to HNCO.

Table 4. Continued.

rac	decl	T_{ex}	N_{HCONH_2}	$N_{CH_3CONH_2}$	N_{HNCO}	$r(CH_3CONH_2/HCONH_2)$	$r(HCONH_2/HNCO)$
"	"	K	$\times 10^{14} cm^{-2}$	$\times 10^{13} cm^{-2}$	$\times 10^{15} cm^{-2}$	%	%
-90	-30	16.6±12.8	0.4±0.2	≤ 0.4	1.9±0.9	≤ 10.8	2.0
-90	-60	19.4±26.0	0.4±0.3	≤ 0.5	1.5±1.1	≤ 14.4	2.4
0	120	7.1±1.4	0.3±0.1	≤ 0.6	1.9±0.5	≤ 16.8	1.8
30	120	6.2±0.2	0.3±0.0	≤ 1.0	2.2±0.1	≤ 28.5	1.6
60	120	7.6±1.1	0.2±0.1	≤ 0.7	1.6±0.3	≤ 32.2	1.5
-30	-120	14.7±4.4	0.5±0.1	≤ 0.4	1.2±0.2	≤ 8.0	4.4
0	-120	13.2±3.9	1.0±0.3	1.4±0.6	1.6±0.4	14.4	6.2
30	-120	12.4±3.5	0.7±0.2	0.9±0.4	1.1±0.3	12.4	6.5
60	60	11.4±2.1	1.0±0.2	1.9±0.6	3.0±0.5	19.2	3.3
-60	60	14.5±6.3	0.6±0.2	1.1±0.7	2.3±0.7	19.6	2.4
60	-60	15.8±5.7	0.6±0.2	0.6±0.3	1.0±0.2	10.7	5.5
60	-120	21.6±30.1	0.5±0.5	≤ 0.7	1.3±0.9	≤ 12.5	4.0
0	-150	18.1±18.3	0.8±0.6	1.1±1.2	1.5±0.9	12.9	5.4
30	-150	12.1±6.6	0.6±0.3	0.8±0.7	1.1±0.5	13.8	5.0
0	-180	14.1±8.8	0.5±0.3	≤ 0.6	1.7±0.8	≤ 11.5	3.0
30	-180	12.2±7.7	0.4±0.2	≤ 0.4	1.0±0.5	≤ 11.9	3.7

APPENDIX

Table A1. The integrated intensities, the first moment (v_{m1} , the intensity-weighted velocity) and second moment (σ_{m2} , the intensity-weighted velocity dispersion) of the transitions of HCONH₂.

rac	dec	4 _{3,2} -3 _{3,1} and 4 _{3,1} -3 _{3,0}			1 _{1,1} -0 _{0,0}			4 _{0,4} -3 _{0,3}		
		intensity	v_{m1}	σ_{m2}	intensity	v_{m1}	σ_{m2}	intensity	v_{m1}	σ_{m2}
"	"	K km s ⁻¹	km s ⁻¹	km s ⁻¹	K km s ⁻¹	km s ⁻¹	km s ⁻¹	K km s ⁻¹	km s ⁻¹	km s ⁻¹
(1)	(2)	(3)	(4)	(5)	(6)	(7)	(8)	(9)	(10)	(11)
-60.0	-60.0	0.9±0.1	57.4	18.4	2.2±0.1	62.3	17.1	7.7±0.1	63.6	21.1
30.0	0.0	1.7±0.1	67.2	24.3	0.8±0.0	65.3	14.8	4.2±0.1	69.6	21.1
-30.0	0.0	5.2±0.1	63.8	15.9	3.0±0.1	69.2	16.8	14.9±0.1	69.9	16.0
0.0	30.0	2.7±0.1	64.7	18.4	3.7±0.1	70.4	20.6	10.8±0.1	69.5	17.9
0.0	-30.0	6.7±0.1	59.3	14.5	1.3±0.1	64.6	15.8	0.0±0.0	61.6	29.2
-30.0	30.0	1.3±0.1	63.0	14.5	3.7±0.1	68.0	17.9	11.5±0.1	69.2	14.6
-30.0	-30.0	5.5±0.1	58.8	23.4	3.7±0.1	65.4	19.9	18.2±0.1	64.5	21.6
30.0	30.0	1.2±0.1	64.8	18.4	3.9±0.0	68.6	22.2	9.6±0.1	69.6	23.1
30.0	-30.0	1.9±0.0	61.7	19.5	0.7±0.1	62.1	16.4	4.0±0.1	65.2	19.0
0.0	60.0	1.0±0.1	64.1	17.2	4.1±0.1	67.8	21.4	13.1±0.1	68.6	20.6
60.0	0.0	0.4±0.1	56.0	13.0	1.0±0.1	62.3	18.1	1.6±0.1	60.5	13.8
-60.0	0.0	0.8±0.1	61.3	15.9	2.7±0.1	66.2	20.7	8.9±0.1	67.8	20.6
0.0	-60.0	7.1±0.1	58.9	15.9	2.1±0.1	62.4	18.0	10.7±0.1	59.5	15.3
30.0	60.0	1.2±0.1	65.2	22.5	4.3±0.1	66.7	19.7	15.0±0.1	68.2	24.4
-30.0	60.0	0.3±0.1	64.7	13.0	2.5±0.1	67.2	18.0	7.1±0.1	66.6	16.6
60.0	30.0	0.6±0.1	60.0	17.2	2.5±0.1	62.7	19.1	5.0±0.1	63.7	16.6
-60.0	30.0	0.7±0.1	60.8	20.5	3.2±0.1	68.1	17.6	9.4±0.1	69.4	20.1
60.0	-30.0	≤ 0.2	57.3	22.5	0.7±0.1	57.2	17.7	3.0±0.1	58.4	17.9
-60.0	-30.0	1.3±0.1	56.5	21.5	3.0±0.1	63.0	20.2	10.3±0.1	63.4	22.6
30.0	-60.0	1.7±0.1	58.2	21.5	1.3±0.1	60.6	19.1	4.0±0.1	59.2	13.0
-30.0	-60.0	5.1±0.1	56.0	20.5	4.0±0.1	63.4	19.8	20.5±0.1	61.1	22.6
-90.0	0.0	≤ 0.2	58.2	0.0	1.3±0.1	63.9	22.4	4.0±0.1	68.2	19.6
0.0	90.0	0.4±0.0	58.7	17.2	3.0±0.1	62.1	20.9	11.1±0.1	61.2	19.6
0.0	-90.0	2.6±0.1	55.0	17.2	3.0±0.1	58.8	17.3	15.6±0.1	56.9	21.1
60.0	90.0	≤ 0.2	60.1	22.5	2.3±0.1	60.4	22.1	9.8±0.1	61.7	20.6
30.0	90.0	≤ 0.2	53.5	18.4	3.1±0.1	63.2	22.4	10.3±0.1	60.8	19.6
-30.0	90.0	≤ 0.2	55.9	18.4	2.0±0.1	61.8	18.6	8.8±0.1	61.3	13.0
-60.0	90.0	≤ 0.2	63.6	0.0	1.4±0.1	62.1	19.7	3.3±0.1	62.8	17.3
-90.0	90.0	≤ 0.2	44.1	0.0	1.5±0.1	60.4	20.4	3.9±0.1	62.3	17.9
60.0	-90.0	0.4±0.1	62.8	18.4	1.6±0.1	60.7	15.1	3.7±0.1	62.2	17.3
30.0	-90.0	1.0±0.1	55.2	20.5	1.4±0.1	61.0	17.3	5.9±0.1	57.8	13.8
-30.0	-90.0	1.7±0.1	55.6	22.5	3.0±0.1	61.3	18.7	13.4±0.1	59.5	20.1
-60.0	-90.0	≤ 0.2	63.3	18.4	1.2±0.1	62.1	20.3	4.4±0.1	60.4	19.6
-90.0	-90.0	≤ 0.2	56.6	0.0	0.9±0.1	64.3	14.0	3.0±0.1	59.5	20.6
-90.0	30.0	≤ 0.2	67.7	14.5	2.0±0.1	72.7	17.4	6.2±0.1	71.9	16.6
-90.0	60.0	≤ 0.2	63.4	14.5	1.5±0.1	66.1	18.7	5.5±0.1	69.1	13.8
-120.0	0.0	≤ 0.3	-78.5	0.0	1.2±0.1	62.1	24.7	3.7±0.1	64.0	28.8
-120.0	30.0	≤ 0.2	58.4	27.6	2.0±0.1	62.8	22.7	4.9±0.1	63.7	24.0
-120.0	60.0	≤ 0.2	53.7	19.5	1.5±0.1	61.1	19.4	4.0±0.1	60.3	22.1
-90.0	-30.0	≤ 0.2	57.1	13.0	1.4±0.1	65.5	20.2	3.7±0.1	64.0	16.6
-120.0	-30.0	≤ 0.2	54.5	0.0	0.9±0.1	68.3	24.5	3.0±0.1	62.4	31.3

Table A1 continued on next page

Table A1 (*continued*)

rac	dec	4 _{3,2} -3 _{3,1} and 4 _{3,1} -3 _{3,0}			1 _{1,1} -0 _{0,0}			4 _{0,4} -3 _{0,3}		
		intensity	v_{m1}	σ_{m2}	intensity	v_{m1}	σ_{m2}	intensity	v_{m1}	σ_{m2}
"	"	K km s ⁻¹	km s ⁻¹	km s ⁻¹	K km s ⁻¹	km s ⁻¹	km s ⁻¹	K km s ⁻¹	km s ⁻¹	km s ⁻¹
(1)	(2)	(3)	(4)	(5)	(6)	(7)	(8)	(9)	(10)	(11)
-90.0	-60.0	≤ 0.2	54.6	18.4	0.9±0.1	64.0	16.2	2.8±0.1	62.8	9.2
-120.0	-60.0	≤ 0.2	60.8	22.5	≤ 0.2	59.1	24.2	1.8±0.1	61.9	19.6
0.0	120.0	≤ 0.2	61.6	27.6	1.0±0.1	61.0	19.6	5.6±0.1	49.5	38.0
30.0	120.0	≤ 0.3	51.1	27.6	1.1±0.2	58.8	33.4	5.9±0.1	49.8	38.0
60.0	120.0	≤ 0.3	55.0	47.7	1.3±0.1	61.5	23.5	3.9±0.1	59.2	24.0
90.0	90.0	≤ 0.2	56.5	42.6	1.0±0.1	57.8	15.4	3.4±0.1	57.7	13.8
90.0	60.0	≤ 0.2	0.0	0.0	1.7±0.1	58.9	28.2	0.0±0.0	53.5	25.3
90.0	120.0	≤ 0.2	49.6	0.0	≤ 0.2	60.3	13.1	2.2±0.1	61.5	16.0
-30.0	-120.0	0.6±0.1	54.8	22.5	1.3±0.1	58.9	20.6	5.8±0.1	60.0	21.1
0.0	-120.0	1.2±0.1	51.9	17.2	2.4±0.1	58.4	18.6	12.0±0.1	57.2	16.0
30.0	-120.0	0.8±0.1	50.1	18.4	1.5±0.1	56.1	11.6	8.4±0.1	55.7	10.3
60.0	60.0	0.9±0.1	61.5	17.2	3.4±0.1	63.8	19.8	13.2±0.1	61.8	22.1
0.0	0.0	22.3±0.2	61.7	15.9	0.0±0.0	67.8	6.7	0.0±0.0	61.5	0.0
-60.0	60.0	≤ 0.3	64.9	25.2	2.3±0.1	67.8	18.7	5.9±0.1	68.8	13.0
60.0	-60.0	0.8±0.1	56.7	22.5	1.7±0.1	57.4	17.5	4.5±0.1	58.0	17.9
30.0	150.0	≤ 0.2	63.4	0.0	≤ 0.3	61.7	14.6	0.8±0.1	60.3	11.3
60.0	-120.0	≤ 0.2	53.9	26.0	1.5±0.1	58.3	18.6	3.6±0.1	57.4	16.0
0.0	-150.0	≤ 0.2	58.6	20.5	1.4±0.1	60.3	16.1	7.3±0.1	60.1	18.5
30.0	-150.0	≤ 0.2	52.4	18.4	1.0±0.1	56.1	12.9	6.7±0.1	55.6	15.3
0.0	-180.0	≤ 0.2	55.6	22.5	1.8±0.1	55.2	16.5	5.9±0.1	55.5	14.6
30.0	-180.0	≤ 0.2	50.7	11.3	1.0±0.1	52.6	14.2	4.4±0.1	51.7	14.6
0.0	-48.0	7.2±0.1	59.6	17.2	0.9±0.1	63.6	18.4	0.0±0.0	54.4	33.3

Table A2. The integrated intensities, the first moment (v_{m1} , the intensity-weighted velocity) and second moment (σ_{m2} , the intensity-weighted velocity dispersion) of the transitions of HCONH₂.

rac	dec	$4_{1,3-3_{1,2}}$			$4_{2,2-3_{2,1}}$			$4_{2,3-3_{2,2}}$		
		intensity	v_{m1}	σ_{m2}	intensity	v_{m1}	σ_{m2}	intensity	v_{m1}	σ_{m2}
"	"	K km s ⁻¹	km s ⁻¹	km s ⁻¹	K km s ⁻¹	km s ⁻¹	km s ⁻¹	K km s ⁻¹	km s ⁻¹	km s ⁻¹
(1)	(2)	(3)	(4)	(5)	(6)	(7)	(8)	(9)	(10)	(11)
-60.0	-60.0	9.7±0.1	63.1	22.2	2.9±0.1	61.7	14.5	3.0±0.1	62.9	15.9
30.0	0.0	6.6±0.1	69.7	23.1	3.0±0.1	69.8	23.4	2.9±0.1	70.0	24.3
-30.0	0.0	19.8±0.1	69.7	19.4	9.2±0.1	68.5	13.0	9.0±0.1	68.6	19.5
0.0	30.0	13.4±0.1	69.0	22.2	5.2±0.1	68.2	19.4	5.1±0.1	68.5	19.5
0.0	-30.0	13.7±0.1	63.5	25.5	10.0±0.1	63.0	24.3	9.9±0.1	63.1	21.6
-30.0	30.0	14.0±0.1	68.4	18.3	4.6±0.1	67.9	15.9	4.7±0.0	68.4	17.2
-30.0	-30.0	25.0±0.1	64.4	24.7	11.8±0.1	62.9	17.1	12.3±0.1	63.9	22.5
30.0	30.0	12.8±0.1	68.9	22.6	4.5±0.1	67.0	24.3	4.3±0.1	68.8	21.6
30.0	-30.0	6.0±0.1	65.1	20.8	3.2±0.1	65.8	14.5	3.5±0.1	66.4	17.2
0.0	60.0	14.3±0.1	68.8	21.3	4.2±0.1	68.5	17.1	4.1±0.1	69.5	24.3
60.0	0.0	3.3±0.1	63.6	28.1	1.0±0.1	64.9	13.0	0.9±0.1	66.9	26.0
-60.0	0.0	10.9±0.1	67.4	21.3	3.1±0.1	67.2	20.5	3.1±0.1	67.3	24.3
0.0	-60.0	17.0±0.1	60.4	16.6	10.2±0.1	61.4	17.1	9.9±0.1	61.4	14.5
30.0	60.0	17.1±0.1	68.3	20.3	5.0±0.1	67.4	20.5	5.1±0.1	69.0	19.5
-30.0	60.0	8.1±0.1	66.8	18.8	2.3±0.1	67.0	18.3	2.2±0.1	66.4	20.6
60.0	30.0	6.6±0.1	63.7	20.3	1.9±0.0	63.7	17.1	1.8±0.1	64.2	19.5
-60.0	30.0	11.3±0.1	68.6	20.3	3.2±0.1	68.0	11.2	3.0±0.1	68.0	20.6
60.0	-30.0	3.9±0.1	58.0	20.3	1.3±0.1	59.2	17.1	1.4±0.1	60.2	22.5
-60.0	-30.0	12.7±0.1	63.4	22.2	4.1±0.1	62.2	20.5	4.0±0.1	63.0	19.5
30.0	-60.0	6.5±0.1	59.8	21.3	2.8±0.1	60.9	18.3	2.6±0.1	60.7	19.5
-30.0	-60.0	26.4±0.1	61.4	21.3	12.0±0.1	60.2	23.4	12.1±0.1	61.0	23.4
-90.0	0.0	4.2±0.1	67.1	20.3	1.1±0.1	67.0	14.5	0.9±0.1	66.3	20.6
0.0	90.0	10.8±0.2	61.3	20.8	2.5±0.1	59.4	20.5	2.3±0.1	60.3	21.6
0.0	-90.0	19.4±0.1	57.8	17.2	6.9±0.1	58.0	19.4	6.8±0.1	58.2	23.4
60.0	90.0	8.2±0.2	60.6	24.3	2.1±0.1	60.3	23.4	2.0±0.1	62.2	20.6
30.0	90.0	10.7±0.2	60.2	27.0	2.4±0.1	61.0	19.4	2.3±0.1	61.5	24.3
-30.0	90.0	7.6±0.1	61.5	19.9	1.9±0.1	60.5	17.1	1.8±0.1	61.8	13.0
-60.0	90.0	4.2±0.1	62.4	19.4	0.9±0.1	63.5	22.5	0.8±0.1	62.6	22.5
-90.0	90.0	3.7±0.1	60.5	17.8	0.7±0.1	63.1	15.9	0.7±0.1	61.3	14.5
60.0	-90.0	6.1±0.1	63.1	20.3	1.9±0.1	63.5	20.5	1.5±0.1	63.7	14.5
30.0	-90.0	8.7±0.1	58.6	19.9	2.6±0.1	58.9	19.4	2.6±0.1	59.3	20.6
-30.0	-90.0	16.2±0.1	60.4	21.3	5.6±0.1	59.8	19.4	5.3±0.1	59.7	19.5
-60.0	-90.0	5.2±0.1	63.5	21.7	1.2±0.1	63.7	9.2	1.2±0.1	61.5	17.2
-90.0	-90.0	2.7±0.1	65.2	19.4	0.5±0.1	63.2	18.3	0.6±0.1	62.5	20.6
-90.0	30.0	6.3±0.1	71.3	20.8	1.3±0.1	71.0	9.2	1.3±0.1	71.2	17.2
-90.0	60.0	5.7±0.1	68.4	18.3	1.2±0.1	69.0	9.2	1.0±0.1	69.4	11.3
-120.0	0.0	4.0±0.1	64.3	27.7	0.8±0.1	66.1	26.7	0.7±0.1	64.6	24.3
-120.0	30.0	5.1±0.1	63.6	21.3	1.2±0.1	63.2	23.4	0.9±0.1	67.4	25.2
-120.0	60.0	3.7±0.1	62.0	19.9	0.8±0.1	62.5	14.5	0.7±0.1	61.3	23.4
-90.0	-30.0	4.2±0.1	64.0	19.9	1.1±0.1	64.5	11.2	1.0±0.1	60.7	20.6
-120.0	-30.0	2.8±0.1	63.7	30.1	≤ 0.2	67.0	15.9	≤ 0.3	68.8	9.2
-90.0	-60.0	3.5±0.1	63.1	17.8	0.8±0.1	64.3	14.5	0.6±0.1	62.9	11.3
-120.0	-60.0	2.2±0.1	63.0	20.3	≤ 0.2	56.5	13.0	≤ 0.2	63.9	24.3
0.0	120.0	4.0±0.1	55.0	28.1	0.6±0.1	60.2	18.3	0.7±0.1	59.2	15.9
30.0	120.0	3.3±0.1	61.7	18.8	0.7±0.1	46.9	29.0	0.7±0.1	58.7	17.2

Table A2 continued on next page

Table A2 (*continued*)

rac	dec	4 _{1,3} -3 _{1,2}			4 _{2,2} -3 _{2,1}			4 _{2,3} -3 _{2,2}		
		intensity	v_{m1}	σ_{m2}	intensity	v_{m1}	σ_{m2}	intensity	v_{m1}	σ_{m2}
"	"	K km s ⁻¹	km s ⁻¹	km s ⁻¹	K km s ⁻¹	km s ⁻¹	km s ⁻¹	K km s ⁻¹	km s ⁻¹	km s ⁻¹
(1)	(2)	(3)	(4)	(5)	(6)	(7)	(8)	(9)	(10)	(11)
60.0	120.0	2.8±0.1	58.7	20.8	0.4±0.1	49.4	0.0	0.6±0.1	57.3	13.0
90.0	90.0	3.9±0.1	59.4	21.7	0.7±0.1	58.1	9.2	0.7±0.1	60.8	20.6
90.0	60.0	5.9±0.1	57.7	32.0	1.2±0.1	57.1	28.3	1.3±0.1	59.1	29.8
90.0	120.0	2.0±0.1	61.4	11.7	≤ 0.2	62.2	13.0	0.4±0.1	61.3	0.0
-30.0	-120.0	6.0±0.1	60.0	18.8	1.9±0.1	58.4	18.3	1.5±0.1	58.2	17.2
0.0	-120.0	12.6±0.1	57.9	16.0	3.1±0.1	56.8	15.9	3.3±0.1	57.0	15.9
30.0	-120.0	9.0±0.1	56.1	11.7	2.3±0.1	55.3	0.0	2.2±0.1	55.7	13.0
60.0	60.0	13.4±0.1	64.0	22.9	3.7±0.0	63.9	21.5	3.4±0.1	64.5	14.5
0.0	0.0	15.4±0.1	64.7	13.7	18.4±0.2	65.6	11.2	17.0±0.1	65.2	11.3
-60.0	60.0	7.0±0.1	67.9	19.1	2.1±0.0	67.8	20.5	1.6±0.1	69.8	13.0
60.0	-60.0	7.0±0.1	59.2	20.1	2.3±0.0	60.9	19.4	2.0±0.1	59.7	11.3
30.0	150.0	1.3±0.1	61.7	30.4	≤ 0.2	60.0	0.0	≤ 0.2	-72.2	0.0
60.0	-120.0	5.5±0.1	57.3	23.5	1.4±0.1	58.7	11.2	1.2±0.1	57.7	18.4
0.0	-150.0	8.5±0.1	62.2	23.1	2.0±0.1	60.5	18.3	1.8±0.1	60.8	9.2
30.0	-150.0	6.9±0.1	56.1	14.7	1.6±0.1	56.2	9.2	1.4±0.1	56.0	15.9
0.0	-180.0	6.3±0.1	55.7	19.4	1.3±0.1	55.2	19.4	1.6±0.1	56.3	22.5
30.0	-180.0	4.6±0.1	52.3	18.3	0.9±0.1	52.4	13.0	0.9±0.1	52.3	13.0
0.0	-48.0	9.4±0.2	61.5	28.4	8.6±0.1	61.7	18.3	8.6±0.1	61.5	13.0

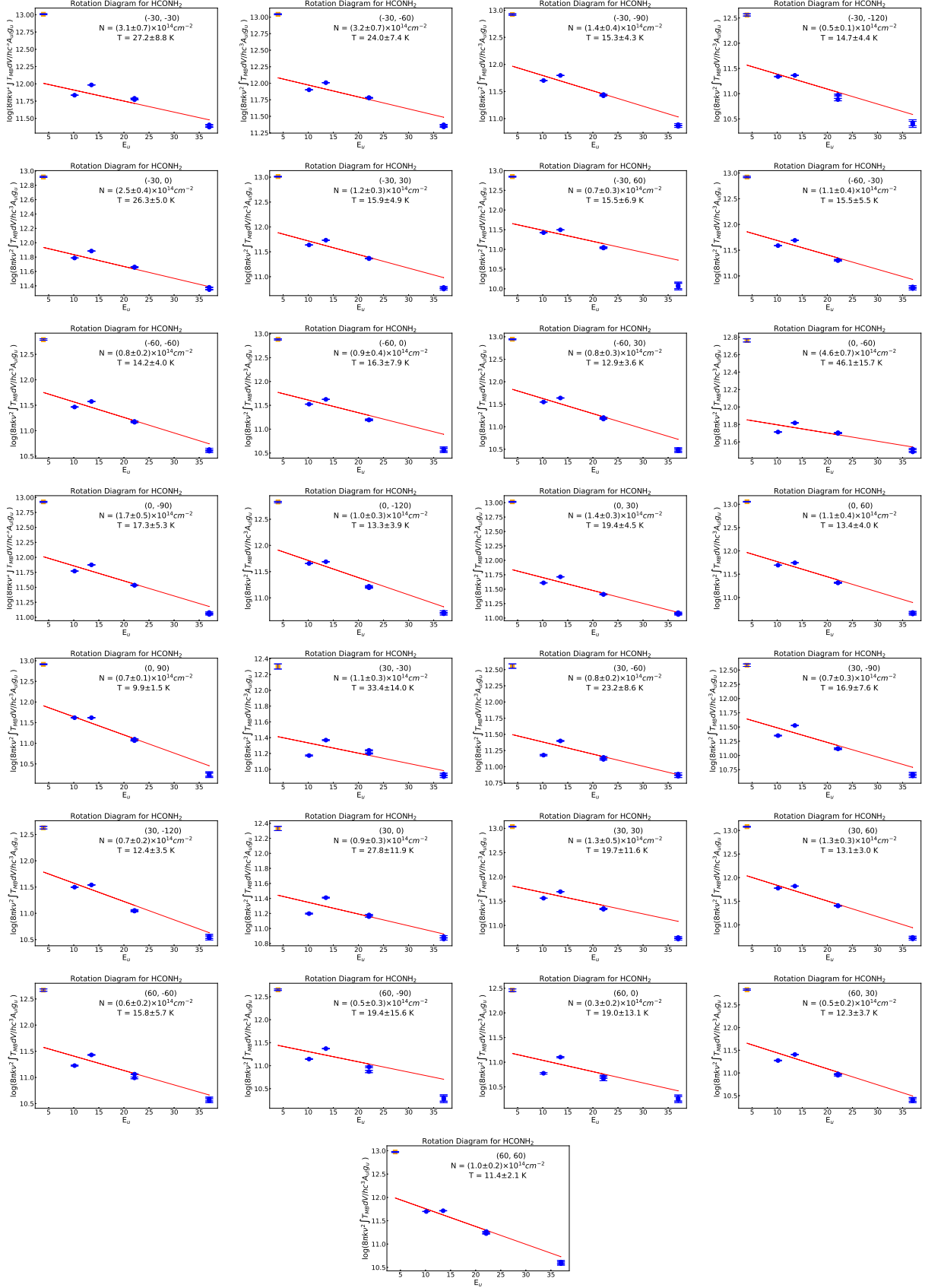


Figure A1. The rotation diagrams of HCONH₂ of positions with HCONH₂ 4₃-3₂ stronger than 3 σ . The error bar is given at 1 σ level. HCONH₂ 1_{1,1}-0_{0,0} is labeled as an orange square, while other transitions are labeled as blue circles.

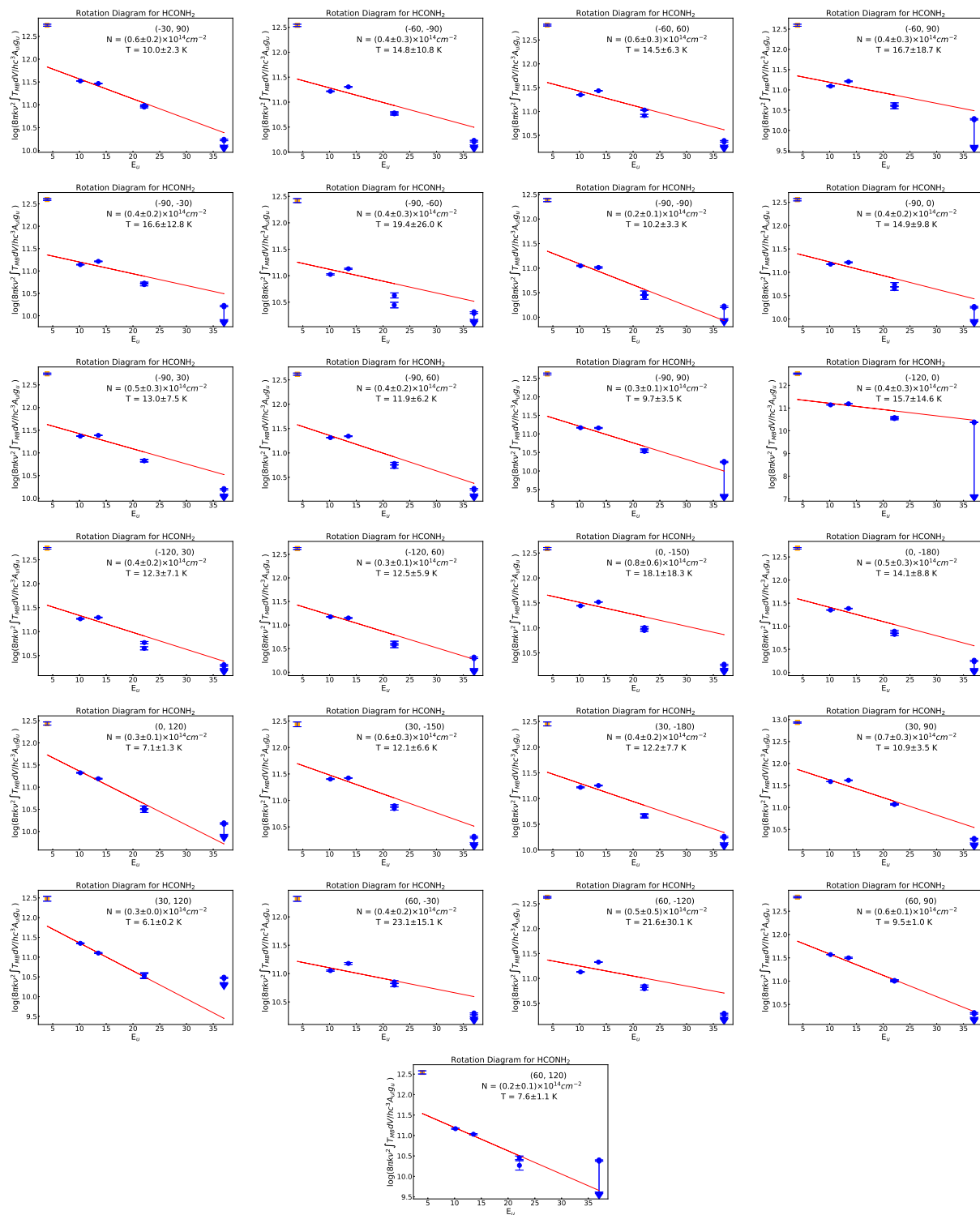


Figure A2. The rotation diagrams of HCONH₂ of positions where HCONH₂ 4₃₋₂ is not detected. The error bar is given at 1 σ level. The downward arrow represents the upper limit of intensity. HCONH₂ 1_{1,1}-0_{0,0} is labeled as an orange square, while other transitions are labeled as blue circles.

REFERENCES

- Barone, V., Latouche, C., Skouteris, D., et al. 2015, *MNRAS*, 453, L31, doi: [10.1093/mnrasl/slv094](https://doi.org/10.1093/mnrasl/slv094)
- Behmard, A., Fayolle, E. C., Graninger, D. M., et al. 2019, *ApJ*, 875, 73, doi: [10.3847/1538-4357/ab0e7b](https://doi.org/10.3847/1538-4357/ab0e7b)
- Belloche, A., Garrod, R. T., Müller, H. S. P., et al. 2019, *A&A*, 628, A10, doi: [10.1051/0004-6361/201935428](https://doi.org/10.1051/0004-6361/201935428)
- Belloche, A., Müller, H. S. P., Menten, K. M., Schilke, P., & Comito, C. 2013, *A&A*, 559, A47, doi: [10.1051/0004-6361/201321096](https://doi.org/10.1051/0004-6361/201321096)
- Belloche, A., Meshcheryakov, A. A., Garrod, R. T., et al. 2017, *A&A*, 601, A49, doi: [10.1051/0004-6361/201629724](https://doi.org/10.1051/0004-6361/201629724)
- Bonfand, M., Belloche, A., Garrod, R. T., et al. 2019, *A&A*, 628, A27, doi: [10.1051/0004-6361/201935523](https://doi.org/10.1051/0004-6361/201935523)
- Bonfand, M., Belloche, A., Menten, K. M., Garrod, R. T., & Müller, H. S. P. 2017, *A&A*, 604, A60, doi: [10.1051/0004-6361/201730648](https://doi.org/10.1051/0004-6361/201730648)
- Cernicharo, J., Marcelino, N., Roueff, E., et al. 2012, *ApJL*, 759, L43, doi: [10.1088/2041-8205/759/2/L43](https://doi.org/10.1088/2041-8205/759/2/L43)
- Codella, C., Ceccarelli, C., Caselli, P., et al. 2017, *A&A*, 605, L3, doi: [10.1051/0004-6361/201731249](https://doi.org/10.1051/0004-6361/201731249)
- Colzi, L., Rivilla, V. M., Beltrán, M. T., et al. 2021, *A&A*, 653, A129, doi: [10.1051/0004-6361/202141573](https://doi.org/10.1051/0004-6361/202141573)
- Du, F., Parise, B., & Bergman, P. 2012, *A&A*, 538, A91, doi: [10.1051/0004-6361/201118013](https://doi.org/10.1051/0004-6361/201118013)
- Ferrero, S., Zamirri, L., Ceccarelli, C., et al. 2020, *ApJ*, 904, 11, doi: [10.3847/1538-4357/abb953](https://doi.org/10.3847/1538-4357/abb953)
- Garrod, R. T. 2013, *ApJ*, 765, 60, doi: [10.1088/0004-637X/765/1/60](https://doi.org/10.1088/0004-637X/765/1/60)
- Garrod, R. T., Wakelam, V., & Herbst, E. 2007, *A&A*, 467, 1103, doi: [10.1051/0004-6361:20066704](https://doi.org/10.1051/0004-6361:20066704)
- Goldsmith, P. F., Lis, D. C., Hills, R., & Lasenby, J. 1990, *ApJ*, 350, 186, doi: [10.1086/168372](https://doi.org/10.1086/168372)
- Gorai, P., Bhat, B., Sil, M., et al. 2020, *ApJ*, 895, 86, doi: [10.3847/1538-4357/ab8871](https://doi.org/10.3847/1538-4357/ab8871)
- Grassi, T., Bovino, S., Caselli, P., et al. 2020, *A&A*, 643, A155, doi: [10.1051/0004-6361/202039087](https://doi.org/10.1051/0004-6361/202039087)
- Halfen, D. T., Ilyushin, V., & Ziurys, L. M. 2011, *ApJ*, 743, 60, doi: [10.1088/0004-637X/743/1/60](https://doi.org/10.1088/0004-637X/743/1/60)
- Halfen, D. T., Woolf, N. J., & Ziurys, L. M. 2017, *ApJ*, 845, 158, doi: [10.3847/1538-4357/aa816b](https://doi.org/10.3847/1538-4357/aa816b)
- Haupa, K. A., Tarczay, G., & Lee, Y.-P. 2019, *Journal of the American Chemical Society*, 141, 11614, doi: [10.1021/jacs.9b04491](https://doi.org/10.1021/jacs.9b04491)
- He, J., Acharyya, K., & Vidali, G. 2016, *ApJ*, 825, 89, doi: [10.3847/0004-637X/825/2/89](https://doi.org/10.3847/0004-637X/825/2/89)
- Henshaw, J. D., Longmore, S. N., Kruijssen, J. M. D., et al. 2016, *MNRAS*, 457, 2675, doi: [10.1093/mnras/stw121](https://doi.org/10.1093/mnras/stw121)
- Herbst, E., & van Dishoeck, E. F. 2009, *ARA&A*, 47, 427, doi: [10.1146/annurev-astro-082708-101654](https://doi.org/10.1146/annurev-astro-082708-101654)
- Hollis, J. M., Lovas, F. J., Remijan, A. J., et al. 2006, *ApJL*, 643, L25, doi: [10.1086/505110](https://doi.org/10.1086/505110)
- Hüttemeister, S., Wilson, T. L., Henkel, C., & Mauersberger, R. 1993, *A&A*, 276, 445
- Hüttemeister, S., Wilson, T. L., Mauersberger, R., et al. 1995, *A&A*, 294, 667
- Ilyushin, V. V., Alekseev, E. A., Dyubko, S. F., Kleiner, I., & Hougen, J. T. 2004, *Journal of Molecular Spectroscopy*, 227, 115, doi: [10.1016/j.jms.2004.05.014](https://doi.org/10.1016/j.jms.2004.05.014)
- Jones, P. A., Burton, M. G., Tothill, N. F. H., & Cunningham, M. R. 2011, *MNRAS*, 411, 2293, doi: [10.1111/j.1365-2966.2010.17849.x](https://doi.org/10.1111/j.1365-2966.2010.17849.x)
- Jones, P. A., Burton, M. G., Cunningham, M. R., et al. 2008, *MNRAS*, 386, 117, doi: [10.1111/j.1365-2966.2008.13009.x](https://doi.org/10.1111/j.1365-2966.2008.13009.x)
- Kryvda, A. V., Gerasimov, V. G., Dyubko, S. F., Alekseev, E. A., & Motiyenko, R. A. 2009, *Journal of Molecular Spectroscopy*, 254, 28, doi: [10.1016/j.jms.2008.12.001](https://doi.org/10.1016/j.jms.2008.12.001)
- Li, J., Shen, Z., Wang, J., et al. 2017, *ApJ*, 849, 115, doi: [10.3847/1538-4357/aa9069](https://doi.org/10.3847/1538-4357/aa9069)
- Li, J., Wang, J., Lu, X., et al. 2021, *ApJ*, 919, 4, doi: [10.3847/1538-4357/ac091c](https://doi.org/10.3847/1538-4357/ac091c)
- Ligterink, N. F. W., Terwisscha van Scheltinga, J., Taquet, V., et al. 2018, *MNRAS*, 480, 3628, doi: [10.1093/mnras/sty2066](https://doi.org/10.1093/mnras/sty2066)
- Ligterink, N. F. W., Ahmadi, A., Luitel, B., et al. 2022, *ACS Earth and Space Chemistry*, 6, 455, doi: [10.1021/acsearthspacechem.1c00330](https://doi.org/10.1021/acsearthspacechem.1c00330)
- López-Sepulcre, A., Balucani, N., Ceccarelli, C., et al. 2019, *ACS Earth and Space Chemistry*, 3, 2122, doi: [10.1021/acsearthspacechem.9b00154](https://doi.org/10.1021/acsearthspacechem.9b00154)
- López-Sepulcre, A., Jaber, A. A., Mendoza, E., et al. 2015, *MNRAS*, 449, 2438, doi: [10.1093/mnras/stv377](https://doi.org/10.1093/mnras/stv377)
- Marin, F., Churazov, E., Khabibullin, I., et al. 2023, *Nature*, 619, 41, doi: [10.1038/s41586-023-06064-x](https://doi.org/10.1038/s41586-023-06064-x)
- Minh, Y. C., Haikala, L., Hjalmarsen, Å., & Irvine, W. M. 1998, *ApJ*, 498, 261, doi: [10.1086/305558](https://doi.org/10.1086/305558)
- Müller, H. S. P., Schlöder, F., Stutzki, J., & Winnewisser, G. 2005, *Journal of Molecular Structure*, 742, 215, doi: [10.1016/j.molstruc.2005.01.027](https://doi.org/10.1016/j.molstruc.2005.01.027)
- Müller, H. S. P., Belloche, A., Xu, L.-H., et al. 2016, *A&A*, 587, A92, doi: [10.1051/0004-6361/201527470](https://doi.org/10.1051/0004-6361/201527470)
- Noble, J. A., Theule, P., Congiu, E., et al. 2015, *A&A*, 576, A91, doi: [10.1051/0004-6361/201425403](https://doi.org/10.1051/0004-6361/201425403)
- Nummelin, A., Bergman, P., Hjalmarsen, Å., et al. 2000, *ApJS*, 128, 213, doi: [10.1086/313376](https://doi.org/10.1086/313376)
- Öberg, K. I., Bottinelli, S., Jørgensen, J. K., & van Dishoeck, E. F. 2010, *ApJ*, 716, 825, doi: [10.1088/0004-637X/716/1/825](https://doi.org/10.1088/0004-637X/716/1/825)

- Penteado, E. M., Walsh, C., & Cuppen, H. M. 2017, *ApJ*, 844, 71, doi: [10.3847/1538-4357/aa78f9](https://doi.org/10.3847/1538-4357/aa78f9)
- Perrero, J., Enrique-Romero, J., Ferrero, S., et al. 2022, *ApJ*, 938, 158, doi: [10.3847/1538-4357/ac9278](https://doi.org/10.3847/1538-4357/ac9278)
- Pillai, T., Wyrowski, F., Hatchell, J., Gibb, A. G., & Thompson, M. A. 2007, *A&A*, 467, 207, doi: [10.1051/0004-6361:20065682](https://doi.org/10.1051/0004-6361:20065682)
- Quan, D., & Herbst, E. 2007, *A&A*, 474, 521, doi: [10.1051/0004-6361:20078246](https://doi.org/10.1051/0004-6361:20078246)
- Quénard, D., Jiménez-Serra, I., Viti, S., Holdship, J., & Coutens, A. 2018, *MNRAS*, 474, 2796, doi: [10.1093/mnras/stx2960](https://doi.org/10.1093/mnras/stx2960)
- Requena-Torres, M. A., Martín-Pintado, J., Martín, S., & Morris, M. R. 2008, *ApJ*, 672, 352, doi: [10.1086/523627](https://doi.org/10.1086/523627)
- Requena-Torres, M. A., Martín-Pintado, J., Rodríguez-Franco, A., et al. 2006, *A&A*, 455, 971, doi: [10.1051/0004-6361:20065190](https://doi.org/10.1051/0004-6361:20065190)
- Rimola, A., Skouteris, D., Balucani, N., et al. 2018, *ACS Earth and Space Chemistry*, 2, 720, doi: [10.1021/acsearthspacechem.7b00156](https://doi.org/10.1021/acsearthspacechem.7b00156)
- Ruaud, M., Loison, J. C., Hickson, K. M., et al. 2015, *MNRAS*, 447, 4004, doi: [10.1093/mnras/stu2709](https://doi.org/10.1093/mnras/stu2709)
- Saladino, R., Botta, G., Pino, S., Costanzo, G., & Di Mauro, E. 2012, *Chem. Soc. Rev.*, 41, 5526, doi: [10.1039/C2CS35066A](https://doi.org/10.1039/C2CS35066A)
- Schmiedeke, A., Schilke, P., Möller, T., et al. 2016, *A&A*, 588, A143, doi: [10.1051/0004-6361/201527311](https://doi.org/10.1051/0004-6361/201527311)
- Scoville, N. Z., Solomon, P. M., & Penzias, A. A. 1975, *ApJ*, 201, 352, doi: [10.1086/153892](https://doi.org/10.1086/153892)
- Skouteris, D., Vazart, F., Ceccarelli, C., et al. 2017, *MNRAS*, 468, L1, doi: [10.1093/mnrasl/slx012](https://doi.org/10.1093/mnrasl/slx012)
- Vastel, C., Ceccarelli, C., Lefloch, B., & Bachiller, R. 2014, *ApJL*, 795, L2, doi: [10.1088/2041-8205/795/1/L2](https://doi.org/10.1088/2041-8205/795/1/L2)
- Vasyunin, A. I., & Herbst, E. 2013, *ApJ*, 769, 34, doi: [10.1088/0004-637X/769/1/34](https://doi.org/10.1088/0004-637X/769/1/34)
- Wang, Y., Du, F., Semenov, D., Wang, H., & Li, J. 2021, *A&A*, 648, A72, doi: [10.1051/0004-6361/202140411](https://doi.org/10.1051/0004-6361/202140411)
- Zeng, S., Jiménez-Serra, I., Rivilla, V. M., et al. 2018, *MNRAS*, 478, 2962, doi: [10.1093/mnras/sty1174](https://doi.org/10.1093/mnras/sty1174)
- Zeng, S., Zhang, Q., Jiménez-Serra, I., et al. 2020, *MNRAS*, 497, 4896, doi: [10.1093/mnras/staa2187](https://doi.org/10.1093/mnras/staa2187)
- Zeng, S., Rivilla, V. M., Jiménez-Serra, I., et al. 2023, *MNRAS*, 523, 1448, doi: [10.1093/mnras/stad1478](https://doi.org/10.1093/mnras/stad1478)
- Zheng, S.-Q., Li, J., Wang, J.-Z., et al. 2022, *Research in Astronomy and Astrophysics*, 22, 035007, doi: [10.1088/1674-4527/ac46a2](https://doi.org/10.1088/1674-4527/ac46a2)